7-1-2015

BUILDING A BETTER TRAINING IMAGE WITH DIGITAL OUTCROP MODELS: THESE GO TO ELEVEN

Alexandra Pickel

Alexandra C Pickel

Candidate

Earth and Planetary Sciences

Department

This thesis is approved, and it is acceptable in quality and form for publication:

Approved by the Thesis Committee:

Gary Weissmann, Chairperson

Louis Scuderi

Bruce Thomson

BUILDING A BETTER TRAINING IMAGE WITH DIGITAL OUTCROP MODELS: THESE GO TO ELEVEN

By

ALEXANDRA C PICKEL

B.S. ENVIRONMENTAL SCIENCE, UNIVERSITY OF NEW MEXICO, 2010

THESIS

Submitted in Partial Fulfillment of the
Requirements for the Degree of

Master of Science

Earth and Planetary Sciences

The University of New Mexico
Albuquerque, New Mexico

July 2015

DEDICATION

To my parents and Dos Equis… cheers

ACKNOWLEDGMENTS

I wish to express my sincere thanks to the following:

- Jed Frechette for the amazing amount of help with all things lidar and the opportunity to beta test so much software (software that assumes the user knows what she is doing!).

- Paul Neville for opening my eyes to the wonderful world of remote sensing.

- Gary Weissmann for finding help when I needed it.

- Louis Scuderi for most helpful discussions about classification and feature extractions.

- Gary, Louis and Bruce for all of your constructive comments.

I greatly appreciate field assistance and data collection efforts by Lauren Massengill, Reyna Banteah, Cody Bodman, Kevin Painter, Vicki Cuddihee, Michael Cuddihee, Patrick Cuddihee, and Leia Pickel. I also appreciate the wonderful officemates/lifetime friends: Sarah Doyle and Kelsey McNamara, thanks, we had the best office for a bit.

I am grateful to UNM Lidar Lab for the equipment and software. Thank you to the Bureau of Land Management for allowing me access to a closed area, and with encountering large groups of armed men playing war games. I am grateful to the Alexander and Geraldine Wanek Graduate Scholarship and the Caswell Silver Fund. Thank you to the best administrative staff on campus, Cindy, Paula,

Mabel, Faith and Ian, you are amazing. Finally, to my coauthors, much gratitude for the work and edits, the manuscript is so much better for you. This material is based upon work supported by SERDP (Strategic Environmental Research and Development Program) under project number ER-1738. Any opinions, findings, and conclusions or recommendations expressed in this material are those of the author(s) and do not necessarily reflect the views of the sponsor.

BUILDING A BETTER TRAINING IMAGE WITH DIGITAL OUTCROP MODELS: THESE GO TO ELEVEN

Alexandra C Pickel

B.S., Environmental Science, University of New Mexico, 2010
M.S., Earth and Planetary Sciences, University of New Mexico, 2015

ABSTRACT

Current standard geostatistical approaches to subsurface heterogeneity studies may not capture realistic facies geometries and fluid flow paths. Multiple-point statistics (MPS) has shown promise in portraying complex geometries realistically; however, realizations are limited by the reliability of the model of heterogeneity upon which MPS relies, that is the Training Image (TI). Attempting to increase realism captured in TIs, a quantitative outcrop analog-based approach utilizing terrestrial lidar and high-resolution, calibrated digital photography is combined with lithofacies analysis to produce TIs.

Terrestrial lidar scans and high-resolution digital imagery were acquired of a Westwater Canyon Member, Morrison Formation outcrop in Ojito Wilderness, New Mexico, USA. The resulting point cloud was used to develop a cm scale mesh. Digital images of the outcrop were processed through a series of photogrammetric techniques to delineate different facies and sedimentary structures. The classified images were projected onto the high-resolution mesh creating a physically plausible Digital Outcrop Model (DOM), portions of which

were used to build MPS TIs. The resulting MPS realization appears to capture realistic geometries of the deposit and empirically honors facies distributions.

TABLE OF CONTENTS

LIST OF FIGURES

LIST OF TABLES

Chapter 1

Introduction

Numerous publications indicate hydraulic property heterogeneity and connectivity are a driving force on subsurface fluid flow; therefore, quantifying these properties is crucial if models are to be accurate. Many attempts have been made to model these integral properties using standard 2-point geostatistics; however, these realizations are doing a less than ideal job of capturing realistic portrayals of heterogeneity and connectivity. Multi-point statistics are a promising new group of algorithms shown to model the spatial characteristics, i.e. heterogeneity and connectivity, with more realism using a Training Image. The purpose of this work was to explore a methodology for a more physically plausible representation of heterogeneity of hydraulic properties by building a realistic Training Image.

Chapter 2 Building a Better Training Image with Digital Outcrop Models has been submitted to Journal of Hydrology Special Publication Groundwater Flow and Transport and is currently in review. A large majority of the work, approximately 85%, research and writing, is mine. Jed Frechette was instrumental in lidar data collection and processing (5%), Alessandro Comunian ran the multiple point geostatistical realizations and wrote a portion of the

manuscript related to the model (5%) and Gary Weissmann edited the manuscript (5%).

The appendices supplement Ch. 2 with additional detail on the workflow that could not be included in a published manuscript. Appendix A Geologic Setting provides a more in-depth look at the regional geology, including sedimentology and stratigraphy. Site-specific geology is addressed in Appendix B, as this was an integral part of the methodology. Appendix B Methodology provides in-depth information regarding the many processing steps and is organized similar to the methodology section in Ch. 2. Appendix B details not only the processing steps, tools, and parameters for each step in this methodology, also included are some "dead-ends", or areas of research that were not used in the final product, but bear mention here. Appendix B is meant to supplement Ch. 2 with more details than what is appropriate for a published paper, but also needs to stand on its own as a readable document; therefore, the reader may notice similarities between the two documents.

Chapter 2

Building a Better Training Image with Digital Outcrop Models

Pickel, A., Frechette, J.D., Comunian, A., and Weissmann, G.S.

Accepted for publication in Journal of Hydrology Special Publication
Groundwater Flow and Transport, 26 June, 2015

1. Introduction

Many studies have shown heterogeneity and connectivity of hydraulic properties of the aquifer exert a profound control on subsurface fluid flow, and quantification of these properties is vital for models to make accurate predictions (e.g., Fogg 1986; Anderson 1989; Bridge 2003; Weissmann et al. 1999; Weissmann et al. 2004; Renard and Allard 2013). However, these attributes are notoriously difficult to characterize and model since subsurface data we can gather are typically sparse and cover a range of nonoverlapping scales. Without understanding and characterizing the heterogeneity and connectivity of hydraulic properties, subsurface flow and transport cannot be reasonably modeled. In sedimentary reservoirs, heterogeneity and connectivity of hydraulic properties are related to sedimentary structure and facies distribution (e.g., Fogg 1986; Anderson 1989; Koltermann and Gorelick 1996; Davis et al. 1997; Klingbeil et al. 1999; Weissmann et al. 1999) and for the past three decades, studies have typically focused on modeling structure and distribution using a variety of 2-

point geostatistical approaches (e.g., Johnson and Dreiss 1989; Goovaerts 1997; Carle et al. 1998; Weissmann and Fogg 1999; Weissmann et al. 1999, 2004; Ritzi 2000). Unfortunately, 2-point geostatistics may not be capturing realistic lithofacies geometries and fluid flow pathways, i.e. connectivity and unit sinuosity (Heinz et al. 2003; Caers and Zhang 2004; Feyen and Caers 2004; Knudby and Carrera 2005; Lee et al. 2007; Klise et al. 2009; Phelps and Boucher 2009; Vassena et al. 2010; Renard and Allard 2013).

Multiple-point statistics (MPS) are a relatively new group of algorithms, proposed by Guardiano and Srivastava (1993), designed to reproduce spatial patterns like connectivity through use of a Training Image (TI). A TI conceptually represents the geometry or patterns of a physical property of interest (e.g. Hu and Chuganova 2008; Maharaja 2008; Boucher 2011). MPS, based on TIs, use a visual approach, where the geometries and spatial configurations are captured by neighborhood statistics rather than the more traditional, analytical statistics, i.e. variograms (Boucher, 2011). The spatial features and measurements from TIs contain possible configurations for a geologic object and relationships between objects. To date, MPS have demonstrated an increased ability to realistically capture geologic patterns (Strebelle 2002; Caers and Zhang 2004; Hu and Chuganova 2008; Klise et al. 2009; Phelps and Boucher 2009; Boucher 2011; Comunian et al. 2012).

Thus far, most academic research has focused on improving MPS algorithms with little attention paid to building or obtaining TIs, choosing data based on how easy it is to work with but not governed by the geologic setting being modeled (Boucher 2011). This is a problem as TIs are an integral, basic requirement of MPS simulation. Many TIs are made from object-based models, which are easy to parameterize (Maharaja 2008), but the facies geometries are difficult to reproduce at multiple scales (Comunian et al. 2012). Additionally, many of the geometries used in object-based models (e.g., spaghetti string shaped channels) are not realistic nor are such geometries found in the sedimentary rock record. For example, channel belts are composed of amalgamated bar forms, not curvilinear channels stuck together. Such representations are popular for constructing training images (e.g., Caers and Zhang 2004; Feyen and Caers 2004; Maharaja 2008; de Vries et al 2009) but are unrealistic for subsurface representations.

Process-based models, e.g. FLUMY (Lopez et al. 2001) and ALLUVSIM (Pyrcz et al. 2009), are also popular but difficult to constrain locally (Hu and Chuganova 2008; Maharaja 2008). In addition, the parameterization of these models represents an additional challenge to the creation of a reliable TI (Comunian et al 2014). Since TIs are repositories for geometric patterns of geology and do not necessarily need to honor a specific geographic locale as

much as property of interest's spatial features, they pair nicely with empirical models derived from outcrop analogs.

Considering the difficulty in obtaining subsurface measurements, many have relied on outcrops as analogs for realistic lithofacies and hydrofacies geometries (e.g. Davis et al. 1997; Whittaker and Teutsch 1999; Heinz et al. 2003; Dai et al. 2005; Falivene et al. 2006; Zappa et al. 2006; Klise et al. 2009; Bayer et al., 2011; Hu et al. 2011; Nichols et al. 2011; Comunian et al. 2012; Weissmann et al. *in press*). Outcrop geology fills a gap in the scales between well logs and seismic data. Traditional outcrop studies were completed manually using photomosaics and, later, laser range finders; however, technological advances in recent years have opened the door to a wide array of high-resolution spatially explicit data collection techniques, including terrestrial lidar and photogrammetry (e.g., Bellian et al. 2005; Enge et al. 2007; Buckley et al. 2008; Weissmann et al. *in press*). Lidar is a laser-based measurement system that can capture the outcrop geometry in three dimensions (e.g. *x, y, z* point cloud) with resolutions ranging from cm to km scales, thus enabling workers to efficiently measure lithofacies geometries and boundaries. Combining a lidar point cloud with digital images and photogrammetric techniques increases the range of measurable physical attributes, geometries and bounding surfaces, and strengthens the digital model overall by adding RGB data to lidar intensity.

The general purpose of this project is to investigate a lidar and photogrammetry methodology for building physically plausible MPS TIs and conditioning data via an outcrop analog study. These data allows for a collection of measurable properties of lithofacies geometry, from lidar, and surface properties, captured with imagery, obtained directly from the outcrop. This methodology can be applied to improving authenticity of TIs and may significantly improve approaches to modeling subsurface heterogeneity of aquifer properties. We use an outcrop of typical fluvial sedimentary rocks (Westwater Canyon Member of the Morrison Formation, New Mexico) to demonstrate this method.

This paper is organized as follows. First, background is provided on DOMs and the geologic setting followed by a site description. The methods section consists of three parts; first data collection and processing; second, architectural element analysis and classification, and last TI generation and MPS realization, with results interspersed throughout. Discussion is followed by suggestions for future work.

2. Background

2.1 Digital Outcrop Models

Lidar first began to appear in the scientific literature approximately 5 decades ago, however it is only within the last 10-15 years terrestrial lidar has

been extensively utilized in combination with outcrop mapping (Fiocco and Smullin 1963; Bellian et al. 2005, Enge et al. 2007, Buckley et al. 2008). The term, Digital Outcrop Model (DOM) (Bellian et al. 2005), was coined to describe these lidar derived outcrop models. A DOM is a spatially constrained, 3D digital map of an outcrop (Bellian et al. 2005; Engle et al. 2007; Buckley et al. 2008; Buckley et al. 2010) built by projecting digital imagery onto a lidar point cloud derived mesh. The use of terrestrial lidar in building a DOM has many benefits; including large coverage, high precision, and relatively quick procurement (e.g. Bellian et al. 2005; Enge et al. 2007; Buckley et al. 2008; Rarity et al. 2013). Researchers recognized DOM functionality as a digital framework for integrating many types of data into geocellular models (e.g. Xu et al. 2000; Pringle et al. 2004; Weissmann et al. *in press*). Lidar derived DOMs have been used for improved quantification in stratigraphic (Bellian et al. 2005) and structural modelling (Rotevatn et al. 2009) as a backbone for petroleum reservoir characterization. Enge et al. (2007) and Buckley et al. (2008) focused on DOM data collection and processing techniques. Klise et al. (2009), Buckley et al. (2010), Rittersbacher et al. (2014), and Weissmann et al (*in press*) quantified facies boundaries and geometries from outcrops, reducing the uncertainty in a subsurface reservoir or aquifer models. Some research has focused on developing semi-automated tools applied to DOMs for feature detection (Viseur et al. 2007), while others are

working toward an automated workflow mining point cloud data for recognizable geometries (Garcia-Selles et al. 2011). Burton et al. (2011) explored using lidar intensity to remotely sense lithology via rock properties, while Nichols et al. (2011) was able to classify outcrop lithology using statistical analysis on the point cloud. Beyond measuring outcrop geometries, Kurz et al (2011) and Hartzell et al. (2014) paired DOMs with hyperspectral imagery to measure chemical compositions for reservoir characterization. Interestingly, there has been very little research on applying DOMs to geostatistics (Rarity 2014) although they seem a natural fit. Research has centered on reducing uncertainty for standard 2-point geostatistical realizations (Fabuel-Perez et al. 2009; Pyles et al. 2010; Burton and Wood 2001; Weissmann et al. *in press*), though Klise et al. (2009) studied solute transport and connectivity characteristics through a multiple point geostatistical realization with data derived from a DOM.

2.2 Geologic Setting

The Westwater Canyon Member of the Morrison Formation is interpreted as a series of large, high-energy braided fluvial deposits composed of vertically stacked sandstone sheets with mudstone beds. This unit discontinuously outcrops for approximately 500 km along the southern and western uplifted margins of the San Juan basin of New Mexico (Turner-Peterson 1986; Miall and

Turner-Peterson 1989; Cowan 1991). Stratigraphically, the Westwater Canyon Member overlies the Recapture Member with a sharp and easy to recognize contact with some local gradational interfingering; and is overlain by the Brushy Basin Member (Turner-Peterson 1986; Baldwin and Rankin 1995). The Westwater Canyon Member is characterized yellowish-gray to tan, pink or light brown, poorly to well sorted, fine to medium-grained, locally conglomeratic sandstone (Turner-Peterson 1986; Baldwin and Rankin 1995; Kernodle 1996). Sedimentary structures include trough and tabular-planar crossbedding, horizontal to low angle laminations locally truncated by scour surfaces lined with clay rip-up clasts (Turner-Peterson 1986; Turner-Peterson and Fishman 1986). At the surface, maximum outcrop thickness is 110 m on the western edge of San Juan Basin, with an average thickness of 60 m. Outcrops display gradual thinning to the north, east and south and abrupt thinning southwest of Gallup, New Mexico. Subsurface thickness increases from approximately 30 m on the north, east and south sides of the basin to about 90 m in the west-central part of San Juan basin (e.g. Kernodle 1996). Grain size decreases in an easterly direction, both above ground and subsurface (Turner-Peterson 1986; Miall and Turner Peterson 1989; Kernodle 1996).

An intensive sedimentological study by Turner-Peterson (1986) identified a locally apparent 2 to 3 fold subdivision of the member, indicating deposition

during three major fluvial episodes. Trough crossbedding indicates a generally northeast flow direction for the lower fluvial unit and a more east to southeast direction for the middle and upper units, although all three units generally display paleoflow from west to east (Turner-Peterson 1986). Campbell (1976) also studied the Westwater Canyon Member and found two units of northeast flowing channel systems incising into each other.

The Westwater Canyon Member is known to be a regionally significant aquifer throughout San Juan Basin (Kelly 1977; Baldwin and Rankin 1995; Kernodle 1996). Yields in the range of 6.3 L/s have been reported in industrial wells, with transmissivity values ranging from 0.4 – 46 m^2/day and pumping rates from 0.4 – 5.4 L/s in municipal wells (e.g. Baldwin and Rankin 1995). In addition to hydrologic importance, Westwater Canyon Member is economically valuable as the main uranium ore-bearing unit of the San Juan Basin (Turner-Peterson and Fishman 1986; McLemore and Chenoweth 2003). From 1947 – 1982, over 94 million kg of U_3O_8 was mined from Westwater Canyon, approximately half of all uranium ore produced from the Morrison Formation during that time (Chenoweth, 1998). In the late 1980's all Morrison Formation uranium mines closed due to low market prices and foreign competition, leaving a large amount of ore unmined, however with in situ mining technology lowering production

costs, mining companies are looking again towards the Westwater Canyon Member.

2.3 Site Description

The study area outcrop for this project is located approximately 50 km north-northwest of Albuquerque, NM, USA, on the eastern edge of Ojito Wilderness, a BLM managed wilderness area along the southeastern border of the San Juan Basin (Figure 1). The outcrop is a natural amphitheater of Westwater Canyon member deposits. The full "Ojito Amphitheater" is approximately 400 m long along the major axis with cliff faces ranging up to 30 m in height; a subset of this area, approximately 100 m long with faces ranging up to 25 m high, was used for the bulk of this project as the full amphitheater would create a dataset too large for analysis using standard computational methods. Two major lithological textural classes are apparent at this outcrop -- a moderately well sorted, fine to medium grained arkosic, bleached sandstone and a clay rip-up-clast conglomerate with a coarse sandy matrix.

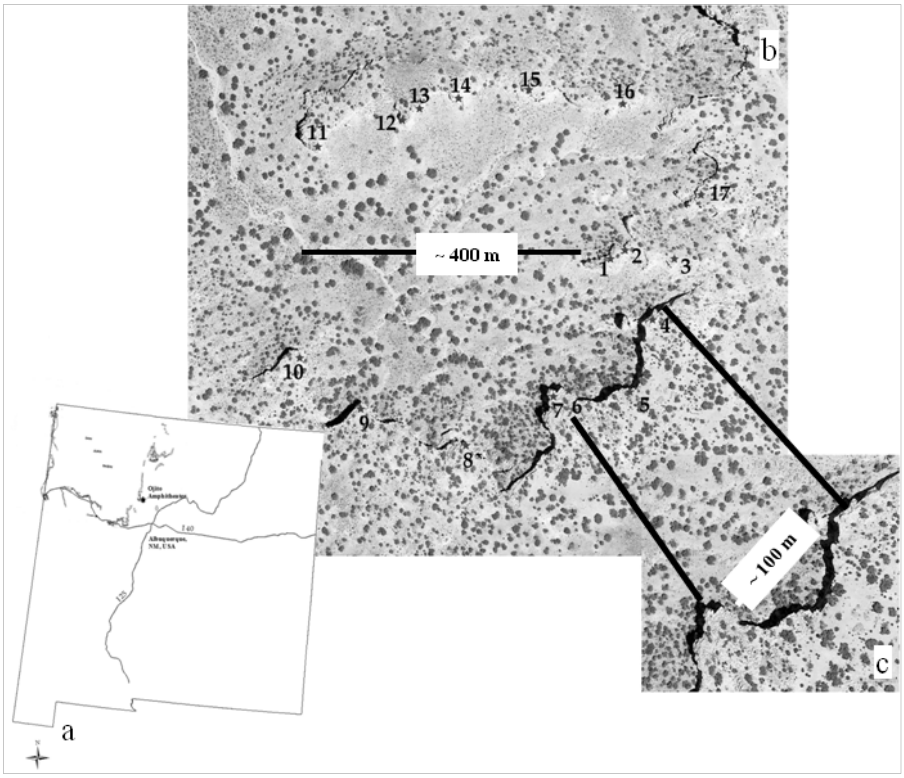

Figure 1. a) Location of Ojito Amphitheater relative to Albuquerque, NM, USA and Westwater Canyon Member outcrop distribution in San Juan Basin, adapted from Miall and Turner-Peterson 1989 b) Google Earth image of Ojito Amphitheater with lidar scan positions c) subset of full amphitheater

3. Methods

3.1 Lidar and Digital Imagery Data Acquisition and Processing

Equipment used included University of New Mexico Lidar Lab's Optech ILRIS-3D terrestrial lidar scanner with pan/tilt base, which uses a 950-nm laser pulsed at 2000-3000 Hz with an exit diameter of 12 mm, beam divergence of 0.17 mrad, and an angular resolution of 26 mrad. Digital imagery was obtained with a Nikon D700 digital camera using a 28-mm fixed lens. Figure 2 outlines the methodology described below.

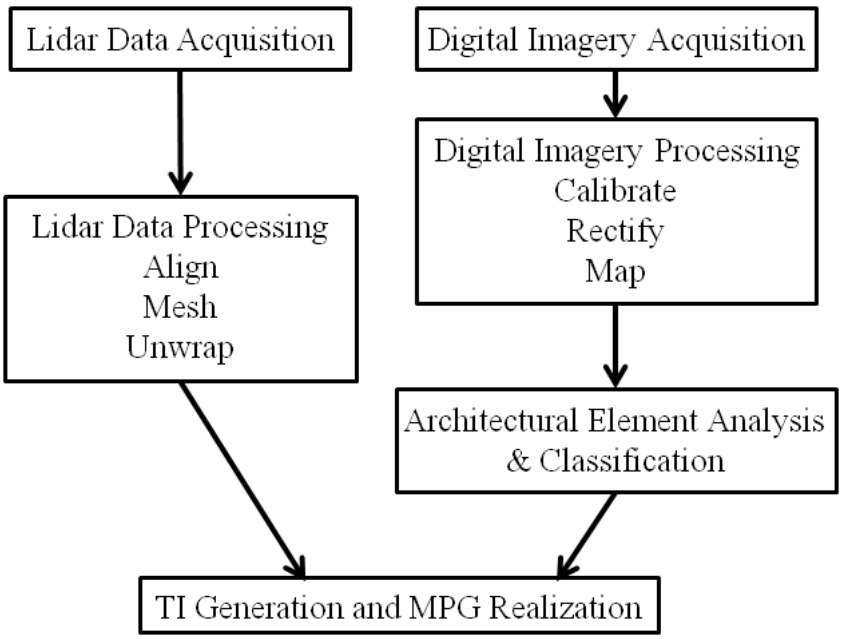

Figure 2. Methodology flow chart

3.1.1 Lidar Data Acquisition

We scanned the full amphitheater, approximately 15 000 m^2 of mostly contiguous cliff face, over a four-day field effort. Seventeen scan positions were required to capture the outcrop exposure geometry (Figure 1). Individual scans were captured with a sampling interval of approximately 5 cm at an average distance of 100 m, however overall point density is significantly higher due to the large amount of overlap between scans. Positions 1 and 12 were globally located using Topcon GR-3 GPS receiver and the remaining fifteen positions were located using a total station survey. All scan positions were registered and georeferenced in NAD83 / UTM zone 13N coordinates (EPSG: 26913) with

orthometric heights referenced to NAVD88 GEOID09 by static GPS and total station control survey.

3.1.2 Digital Imagery Acquisition

Digital imagery was acquired in June 2013 under uniform, diffuse lighting conditions (i.e. overcast days) to take advantage of decreased dynamic range. This decreases any false edges or specular reflections that may arise from shadows and bright areas. Digital imagery was collected in Nikon RAW format to record an accurate measurement of the cliff faces and bypass any in-camera processing. The photographs were collected at arbitrary locations walking around the amphitheater rim with the goal of large overlap and perpendicular views, although given the rugosity of this outcrop it was not always possible to obtain perpendicular views.

3.1.3 Lidar Data Processing

The collected lidar data were first downloaded and preprocessed with the ILRIS-3D Parser, outputting scan files as a 3D digitized data set suitable for future processing steps. Scan alignment was completed in PolyWorks/IMAlign module (v. 11.0.36, Innovmetric Software, Inc) with the best-fit alignment algorithm, an iterative, optimization technique for minimizing 3D distances between surfaces. The files were imported into IMSurvey (v. 11.0.36, Innovmetric Software, Inc) and standard point cloud editing tools were used to

classify all points as either outcrop or non-face points, clipping to just the outcrop area and sub-sampling for a more uniform point cloud density. The edited point cloud was exported as an unorganized point cloud in the form of a space separated, ASCII text file of *x*, *y*, *z* with normal vectors. A Poisson Surface Reconstruction (PSR) was applied, via an IMEdit macro, to create a multiscale, "watertight" mesh from the point cloud (Kazhdan et al., 2006; Kazhdan and Bolitho 2006). The PSR algorithm is global, using all points to create a smooth surface while maintaining integrity to a rugose outcrop surface with locally fitting functions (Kazhdan et al, 2006). The PoissonRecon IMEdit macro has three parameters for mesh creation; octree depth, solver divide, and samples per node. Octree depth is the most important as a control on mesh resolution with greater depths corresponding to higher resolutions. The mesh was generated using an octree depth of 14 on a computer with 24 GB of RAM and a point cloud with just over fourteen million points. Solver divide, second PSR parameter, controls splitting the reconstruction into multiple processes to avoid overworking available RAM, a solver divide of 10 worked well. The third parameter specifies minimum number of points that must be in an octree node, considering the point cloud had been subsampled for uniformity, two samples per node worked well.

UV terminology is used to refer to "texture-space coordinates" instead of x, y, z "3D space"; it is a process of assigning 2D coordinates to the vertices. UV mapping is the process of mapping (projecting) a 2D texture over a 3D object, in our case the digital photographs onto the lidar derived mesh. Before a texture, either photograph or interpreted image, can be projected onto a mesh, the 3D mesh must be converted, or flattened, to 2D, a process known as unwrapping. Similar to cutting a paper model of an object in specific places so that it can lay flat, the mesh can be cut and transformed into a representative 2D system. Each point in the UV map correlates to a vertex in the mesh, UV map lines are mesh edges and UV map faces are mesh faces. Blender (v. 2.73, Blender), an open source 3D computer graphics software, currently has the best tool for unwrapping complicated, dense meshes with their Smart UV Project tool. The Smart UV Project splits the mesh into islands, or groups, based on angular changes in the mesh. Angle limit controls how faces are grouped and refers to the angle between faces; a higher limit results in many small islands with low distortion, lower limits the opposite. An angle limit of 80 worked well, lessening distortion for the dense mesh. Once the mesh is UV mapped and unwrapped, the images can be projected onto it.

3.1.4 Digital Imagery Processing

Before imagery can be mapped onto the mesh, the camera must be calibrated in order to find internal distortion parameters and external parameters describing poses when images were captured. Internal distortion parameters are comprised of both radial distortion, a result of the lens shape, and tangential distortion, a result of the camera's assembly process. External parameters describe the pose of an object relative to the camera and can be defined in terms of rotation, describing a point's location in a new coordinate system, and the translation vector, shifting the origin to the new coordinate system (Bradski and Kaehler 2008).

We chose a calibration procedure based on dense stereo matching, as found in Agisoft PhotoScan (v. 0.9.1, Agisoft PhotoScan). To make the most out of PhotoScan, imagery was transformed from raw format to a scene linear 16-bit floating point OpenEXR format, a high-dynamic-range image file format that allows for better color precision and measurement (www.openexr.com). Using PhotoScan's alignment workflow, images were inspected and tie points manually placed to aid in the alignment process. These tie points also served as 3D ground control points for transforming the coordinate system from arbitrary, local system to 3D, real world coordinate system used by IMSurvey(v. 11.0.36, Innovmetric Software, Inc). Pair preselection was disabled, as images were not always captured continuously. Accuracy was first set lower, and then adjusted

higher once camera poses were roughly approximated. Once calibration parameters were calculated, the scene geometry was reconstructed. The resultant texture, resolution of 0.0615 m/pixel and point density of 52 360 points/m^2, was UV mapped onto the lidar derived mesh.

3.2 Architectural Element Analysis and Classification

Architectural-element analysis (Miall, 1985), a lateral profiling technique, is often applied to understand the distributions of fluvial facies on an outcrop. In addition, fluvial bounding surfaces mapped by this technique provide a framework for integrating geologic information into stochastic models. Some large-scale mapping and analysis suggests fourth order bounding surfaces correspond to large-scale permeability correlation structures (Davis et al. 1997). In the case of Westwater Canyon, architecture of sandstone bodies influences fluid flow and subsequent uranium emplacement (Cowan 1991). The subset outcrop (Figure 1) was studied according to field methodology proposed by Miall (1985) and this information used as the basis for classification.

The digitized images are shown in Figure 3. Five depositional units, labeled B-F, separated by 5^{th} order bounding surfaces, were identified. The lower boundaries are delineated by the clay rip-up-clast conglomerate. Unit B contains the coarser, clay-clast conglomerate facies heavily interbedded with fine sand, displaying a heterolithic unit with some horizontal laminations. Internal

assemblages for Unit C include some low angle crossbeds inside 4th order bounded minor channels, but most sections appear to be massive. Internally, Unit D contains solitary and grouped trough crossbeds, horizontal laminations, low angle crossbeds and one identified very broad, shallow planar crossbedded scour. Unit E's internal geometries and assemblages include multiple scours with low angle crossbeds, some of which are broad and very shallow. Horizontal laminations are associated with the low angle crossbeds. Internally Unit F contains horizontal laminations and multiple 4th order bounded minor channel fill deposits with concave up, scoop shaped bases. Generally, subset outcrop crossbeds primarily indicate southeasterly flow. The massive and low angle to planar bedded facies are fine to lower medium grained sand, while the trough cross bedded facies are fine to upper medium with some coarse grains. Low-angle crossbeds and horizontally-laminated facies are often associated with each other and indicate upper flow regime or a transition from subcritical to supercritical status (Miall, 1996), consistent with a high energy, braided fluvial environment.

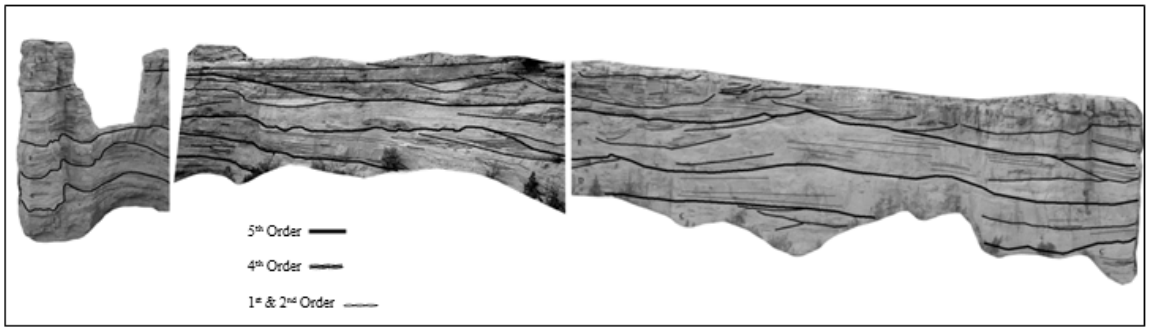

Figure 3. Architectural element analysis, in the style of Miall (1985), of subset amphitheater.

Based on findings from the architectural element analysis, the subset amphitheater was classified into four lithofacies; clay rip-up-clast conglomerate, massively bedded sands, low angle sands, and trough cross-bedded sands with some coarse grains. To digitize the classification on the imagery, traditional photogrammetric classification approaches were employed. Diagonal and horizontal zero-sum edge detection techniques were modified to emphasize the planar, low angle, and trough cross-bedded sands, while color indices were used to distinguish more blue-colored clay rich areas from the surrounding red and tan sandstones (Figure 4a). Classification was manually digitized on the rectified images and then UV mapped onto the mesh to complete the interpreted DOM (Figure 4b).

3.3 Training Image Generation and MPS realization

Comunian at al. (2012) proposed an approach to tackle the lack of a full 3D training image, using a sequence of 2D MPS simulations with conditioning data (s2Dcd method). In the s2Dcd method, simulations are performed along a given

sequence using 2D training images deemed representative, by the user, of the model of heterogeneity along orthogonal directions. At each step, facies codes simulated at the previous steps of the sequence that intersect the current simulation surface are considered as conditioning data. In this way, with a series of 2D simulations, a 3D domain is filled preserving an overall coherence. The s2Dcd requires a MPS simulation engine, and in this study we used (*impala*, Straubhaar et al, 2011). The 2D training images required to perform the s2Dcd approach were obtained by projecting the outcrop data along two orthogonal planes, *xz* and *yz*, approximating the outcrop shape (Figure4b). The interpreted DOM data were discretized on a 10 cm structured grid in GRASS GIS (GRASS Development Team, 2008) with the g.region module, and the sections were projected onto planes using GRASS GIS' r.in.xyz module by importing *y, z* for one image and *x, z* for the second image into the *x, y* columns. The data were then exported using r.out.vtk, for outputting 2D raster maps into vtk-ASCII format consistent with use in *impala*.

Here we first tried using both 2D training images along the *yz* and *xz* directions (Figure4c). The training images present a clear vertical trend. Therefore, to handle this non stationarity, we simulated using the *z* coordinate as an auxiliary variable (Chugunova and Hu, 2008; Straubhaar et al. 2011). However, the 2D training images obtained by projecting the outcrop data along

the *xz* and *yz* planes presents some incoherence, because patterns of heterogeneity observed for a given value of *z* in one TI can hardly be found in the other TI (Figure 4b). As a consequence, the results obtained with this first run of the s2Dcd (Figure 4c) method presents some artifacts, due to the difficulty in finding coherent patterns of heterogeneity between the two considered training images. Less noisy results were obtained by using a single training image and transposing it along both 2D paths. To do this, we took the TI along the *xz* path and transposed it along the *yz* direction. Using this training image the variability of heterogeneity patterns is reduced (and greater coherence between the TIs produces a 3D simulation with much less noise (Figure 4d).

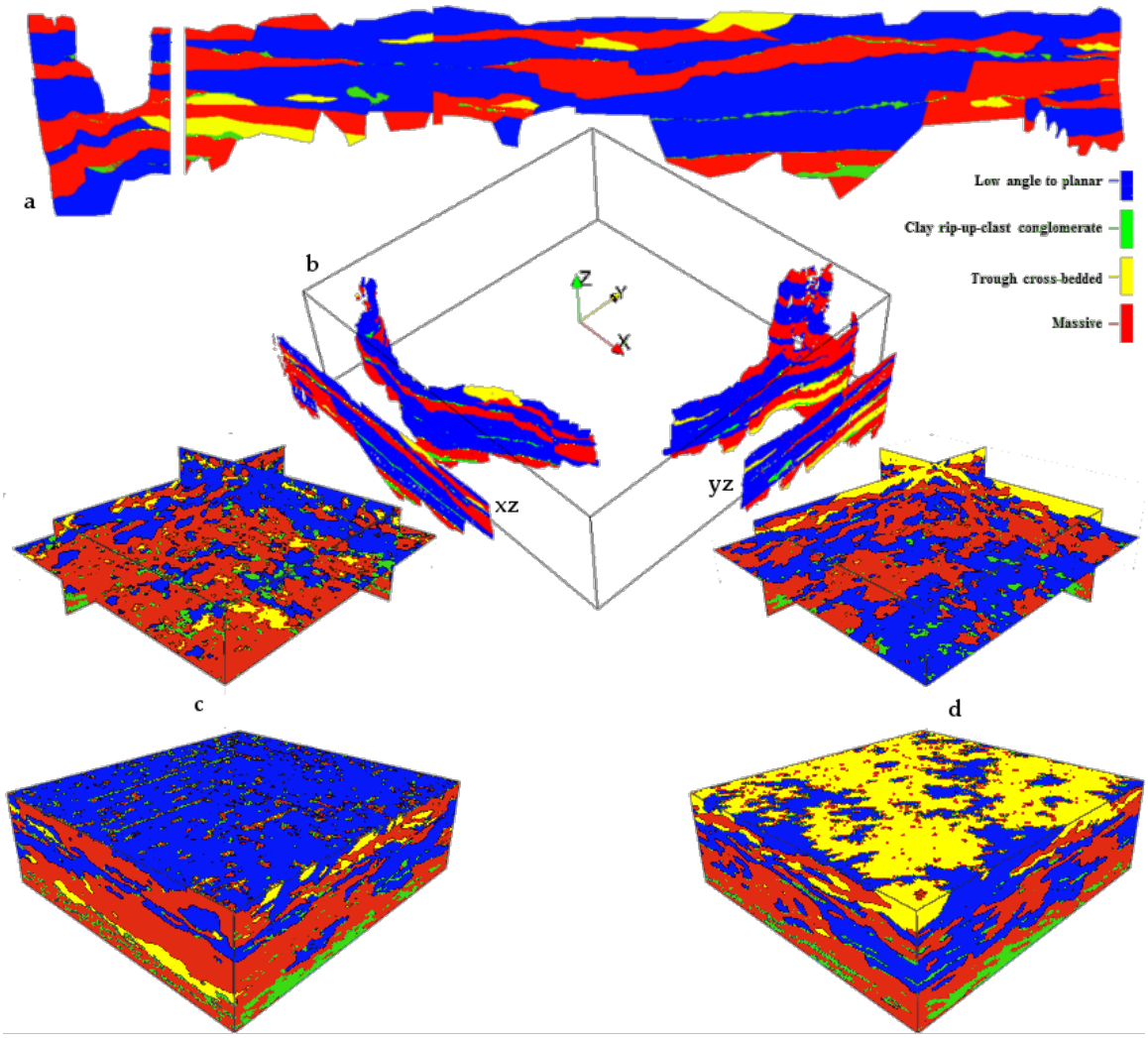

Figure 4. a) Photomosaic of classified images, texture for the interpreted DOM b) 3D and corresponding projected 2D TIs c) s2Dcd simulation results with both 2D TIs using z coordinate as auxiliary variable to cope with nonstationarity d) s2Dcd simulation results with only one 2D TI orthogonally transposed to cope with heterogeneity coherence

4. Discussion and Conclusion

The results show it is possible to build MPS TIs from a DOM, integrating spatial information obtained directly from outcrop measurements, a need clearly indicated in the literature (Dimitrakopoulos et al. 2010; Boucher 2011; Renard and Allard 2013). Models of heterogeneity developed from these TIs appear to

capture facies geometries observed at the study site. An advantage of using outcrop analogues over process-based models or other means to build TIs is accessibility to real world patterns of heterogeneity. DOMs provide accurate information about the relationship between facies distributions, the connectivity of those distributions and realistic body geometries that are representative of actual sedimentary structure. The advantages and disadvantages of lidar as a data collection method are not discussed here, as a growing body of research already exists on this topic (e.g. Hodgetts 2013; Rarity et al. 2013).

However, there are limitations with this dataset. One limiting factor is the similarity in geologic features, or lack of significant heterogeneity, at this site. Due to this we were not able to apply a quantitative classification scheme or make the lithofacies to hydrofacies interpretation, which would have strengthened the interpreted DOM as a TI. The qualitative classification scheme we used was the result of attempting to apply a semi-automated classification technique to the digital images. Currently, research is being conducted to integrate hyperspectral imagery (e.g. Kurz et al. 2011; Hartzell et al 2014), which may be more applicable to automated facies classification than visible light imagery. The qualitative classification scheme was also limiting in that the scales between outcrop structures mapped and the simulation area differed. In other

words, to have statistically homogenous TIs, this classification scheme needs to be mapped on a kilometer scale, not the sub kilometer scale available to us.

For applying standard MPS simulation methods, a training image should have the same dimensionality as the simulation grid, if a simulation is on a 3D domain, then a 3D training image is required. The interpreted DOM (Figure4b) does not have full 3D dimensionality, rather it consists of several approximately 2D slices; however, it does contain many patterns of correlation along diverse orientations and the natural amphitheater shape provides some constraint for modelling physical features, i.e. connectivity, in the third dimension.

One of the limitations of the s2Dcd approach is the assumption regarding symmetry of the heterogeneity in the simulation domain. In the best situation, one 2D training image is available along each simulation direction x, y and z. Moreover, maximum coherence is required among all the training images. Our site does not display maximum coherence between the TIs, as facies juxtaposition differs from one TI to the other. Another difficulty in common with all the other MPS simulation strategies is the non-stationarity of the training image, facies distributions in both TIs display a clear, vertical trend. Here we adjusted for the lack of stationarity using z as an auxiliary variable (Chugunova and Hu, 2008; Straubhaar et al. 2011).

Improvements on this methodology could include building a larger interpreted DOM to account for more heterogeneity and subsequent patterns, using the stratigraphy to break out similar units in a manner similar to that described by Weissmann and Fogg (1999), and including general paleoflow direction in the simulations. Through an approach integrating terrestrial lidar and digital image photogrammetry of an outcrop, we built training images for a multiple point statistical realization that are a step closer to reality.

Appendix A Geologic Setting

The Morrison Formation of Late Jurassic age stretches across much of the western United States, from New Mexico north to Montana and Idaho and east to South Dakota (Turner and Peterson 2004). In New Mexico, it is found throughout the northern half of the state, including the San Juan Basin, a Laramide age, asymmetrical structural basin (Kernodle 1996, Stone 2003) formed as a result of a Late Jurassic Andean-type magmatic arc (Miall and Turner-Peterson 1989; Cowan 1991). An uplifted rift shoulder southwest of the basin formed the Mogollon highlands. This provided the topographic gradient and a potential sediment source for deposition of the Morrison Formation members (Baldwin and Rankin 1995; Turner and Peterson 2004; Dickinson and Gehrels 2008; Laskowski et al. 2013). In New Mexico, the Morrison Formation conformably overlies the Wanaka Formation or Cow Springs Sandstone and is unconformably overlain by Cretaceous age Dakota Sandstone (Turner-Peterson 1986; Miall and Turner-Peterson 1989; Cowan 1991; Kernodle 1996; Turner and Peterson 2004). In the San Juan Basin, the Morrison Formation has a mean thickness of 200 m and consists of five members -- Bluff, Salt Wash, Recapture, Westwater Canyon, and Brushy Basin, with Bluff and Salt Wash Members limited to the San Juan Basin's northwestern portion (Turner-Peterson 1986).

The Salt Wash and Westwater Canyon Members are large, laterally extensive relatively coarse-grained fluvial deposits and the Bluff Member is characterized as an eolian deposit. The Recapture Member is highly heterogeneous comprised of fluvial, lacustrine and eolian deposits, and the Brushy Basin Member also represents a mix of environments, including fluvial, overbank, wetland and lacustrine (Turner-Peterson 1986; Turner-Peterson and Fishman 1986; Cowan 1991; Turner and Peterson 2004). Of the five members, the Westwater Canyon Member displays high transmissivities, making a regionally significant aquifer (Kelly 1977; Baldwin and Rankin 1995; Kernodle 1996), and it contains arguably the most significant uranium ore bearing deposit in the San Juan Basin (Chenoweth 1998; McLemore and Chenoweth 2003).

The Westwater Canyon Member discontinuously outcrops for approximately 500 km along the southern and western uplifted margins of the San Juan basin (Turner-Peterson 1986; Cowan 1991) and is interpreted as a series of large, high energy braided fluvial deposits composed of vertically stacked sandstone sheets with mudstone beds (Turner-Peterson 1986; Miall and Turner-Peterson 1989; Godin 1991). Stratigraphically, the Westwater Canyon Member overlies the Recapture Member with a sharp and easy to recognize contact, though locally this contact may be gradational or interfingering. The Westwater Canyon Member is overlain by the Brushy Basin Member, with a contact

displaying a vertical change from massive cliff forming sandstones to slope forming mudstones and sandstones (Turner-Peterson 1986; Baldwin and Rankin 1995).

The Westwater Canyon Member is characterized by yellowish-gray to tan, pink or light brown, poorly to well sorted, fine to medium-grained, locally conglomeratic sandstone (Turner-Peterson 1986; Baldwin and Rankin 1995; Kernodle 1996). Sedimentary structures include trough and planar-tabular crossbedding, horizontal to low angle laminations locally truncated by scour surfaces lined with clay rip-up clasts (Turner-Peterson 1986; Turner-Peterson and Fishman 1986). At the surface, maximum outcrop thickness is 110 m on the western edge of San Juan Basin, with an average thickness of 60 m. Outcrops display gradual thinning to the north, east and south and abrupt thinning southwest of Gallup. Subsurface thickness increases from approximately 30 m on the north, east and south sides of the basin to about 90 m in the west-central part of San Juan basin (e.g. Kernodle 1996). A general grain size decrease is observed in an easterly direction in both surface exposures and in the subsurface (Turner-Peterson 1986; Miall and Turner Peterson 1989; Kernodle 1996).

An intensive sedimentological study by Turner-Peterson (1986) identified a locally apparent 2 to 3 fold subdivision of the Westwater Canyon Member, with all 3 units well-defined along the west side of the basin. The middle unit,

however, thins toward the south and east and only the upper and lower fluvial units can be seen in the southeast portion of the basin (the study area for this thesis). This indicates deposition during three major fluvial episodes, the first and last resulting in laterally extensive sandstone sheets. Trough crossbedding indicates a generally northeast flow direction for the lower fluvial unit and a more east to southeast direction for the middle and upper units, although all three units generally display paleocurrents with a west to east direction (Turner-Peterson 1986). Campbell (1976) also studied the Westwater Canyon Member and described two units of northeast flowing channel systems incising into each other. Campbell based these findings on an east-west fluvial system transect thought to be approximately perpendicular to regional paleoflow, but Turner-Peterson (1986) has shown this transect to be all but parallel to paleoflow.

The Westwater Canyon Member is known to be a regionally significant aquifer throughout San Juan Basin (Kelly 1977; Baldwin and Rankin 1995; Kernodle 1996). Yields in the range of 6.3 L/s have been reported in industrial wells, with transmissivity values ranging from 0.4 – 46 m^2/day and pumping rates from 0.4 – 5.4 L/s in municipal wells (e.g. Baldwin and Rankin 1995). In addition to hydrologic importance, the Westwater Canyon Member is economically valuable as the main uranium ore-bearing unit of the San Juan Basin (Turner-Peterson and Fishman 1986; McLemore and Chenoweth 2003).

From 1947 – 1982, over 94 million kg of U_3O_8 was mined from Westwater Canyon, approximately half of all uranium ore produced from the Morrison Formation during that time (Chenoweth, 1998). In the late 1980's all Morrison Formation uranium mines closed due to low market prices and foreign competition, leaving a large amount of ore unmined, however with in situ mining technology lowering production costs, mining companies are looking again towards the Westwater Canyon Member.

Appendix B Methods

1. Lidar and Digital Imagery Data Acquisition and Processing

Equipment used included University of New Mexico Lidar Lab's Optech ILRIS-3D terrestrial lidar scanner with pan/tilt base, which uses a 950-nm laser pulsed at 2000-3000 Hz with an exit diameter of 12 mm, beam divergence of 0.17 mrad, and an angular resolution of 26 mrad. The pan/tilt base expands the scan area from just one scan window, enabling scanning across a full 360º horizontally and up to 70º tilt. Digital imagery was obtained with a Nikon D700 digital camera using a 50-mm and 28-mm fixed lens. Real world coordinates were obtained with a Topcon GR-3 GPS Receiver and Total Station. Figure B1 outlines the methodology described below.

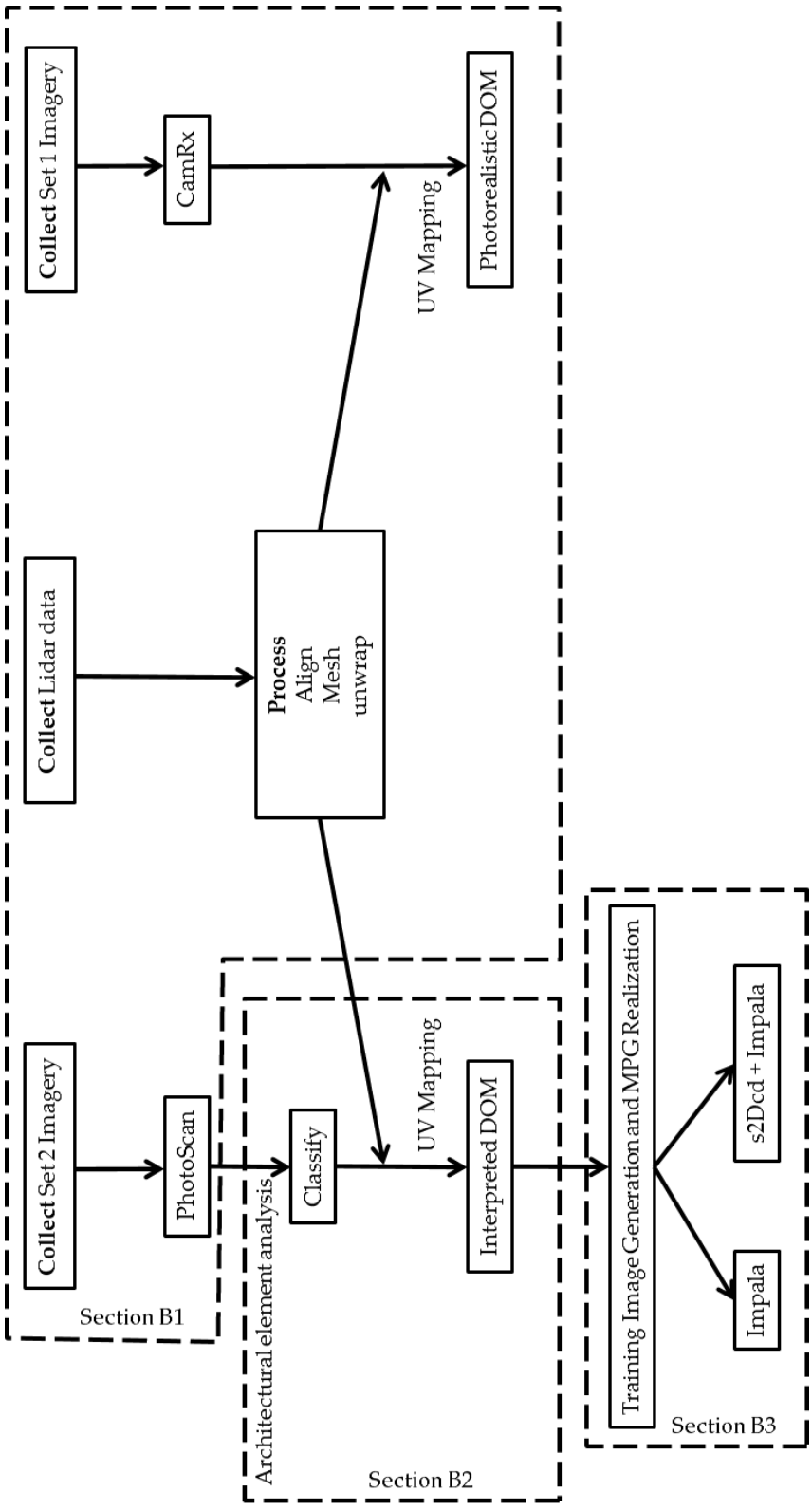

Figure B1. Lidar and photographic data acquisition and processing flow chart

1.1 Lidar Data Acquisitions

We scanned approximately 15,000 m^2 of mostly contiguous cliff face over a four-day field effort in May 2011. Seventeen scan positions were required to capture the outcrop exposure geometry (Figure B2 and Table B1). At positions OJA03, OJA04, OJA06, OJA11, OJA13, and OJA14, the outcrop area scanned, known as Region of Interest (ROI), fit inside one scan window and thus the pan/tilt base was not needed. All other positions had ROIs larger than one scan window, necessitating use of the pan/tilt base, thus resulting in multiple subgroups per these scanner positions. Scans were captured with a sampling interval of approximately 5 cm at an average of a 100-m range, however overall point density is significantly higher due to the large amount of overlap between scans. Positions 1 and 12 were globally located using Topcon GR-3 GPS receiver and remaining fifteen positions were located with total station survey. All scan positions were registered and georeferenced in NAD83 / UTM zone 13N coordinates (EPSG: 26913) with orthometric heights referenced to NAVD88 GEOID09 by static GPS and total station control survey.

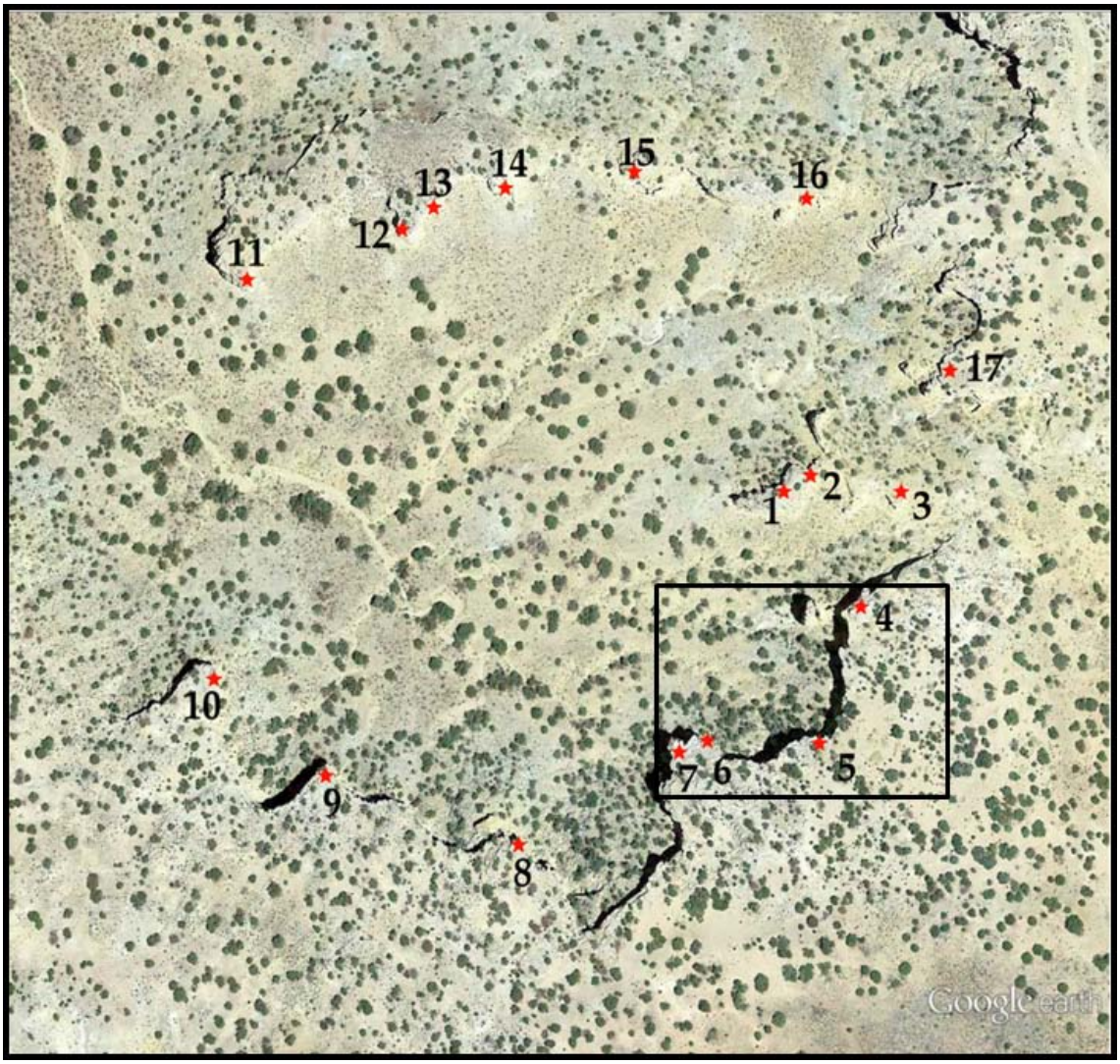

Figure B2. Google Earth image of Ojito Amphitheater, red stars mark scan positions, subset study area in box

Table B1. Station Field Data

							Huge Translation		
							329870	3932572	1675
Station ID	Date	Easting	Northing	Ortho Height	z-offset (m)	Adjusted Ortho Height	x Translation	y Translation	z Translation
OJA01	20110517	330280.437	3932838.2	1786.391	1.707	1788.098	410.437	266.199	111.391
OJA02	20110526	330295.004	3932852.01	1786.233	1.332	1787.565	425.004	280.013	111.233
OJA03	20110517								
OJA04	20110517	330355.755	3932804.4	1788.795	1.1402	1789.9352	485.755	232.398	113.795
OJA05	20110517	330318.043	3932780.37	1788.108	1.19	1789.298	448.043	208.372	113.108
OJA06	20110523	330290.4	3932718.34	1786.518	1.185	1787.703	420.4	146.336	111.518
OJA07	20110523	330233.916	3932717.07	1786.35	1.42	1787.77	363.916	145.073	111.35
OJA08	20110523	330220.002	3932714.6	1786.002	1.515	1787.517	350.002	142.599	111.002
OJA09	20110523	330127.257	3932672.21	1783.754	1.185	1784.939	257.257	100.205	108.754
OJA10	20110523	329970.524	3932768.99	1779.188	1.184	1780.372	100.524	196.987	104.188
OJA11	20110523	330025.843	3932712.64	1779.347	1.333	1780.68	155.843	140.644	104.347
OJA12	20110524	329999.684	3932981.35	1775.355	1.544	1776.899	129.684	409.347	100.355
OJA13	20110524	330089.747	3932999.05	1781.141	1.047	1782.188	219.747	427.053	106.141
OJA14	20110524	330105.962	3933005.72	1781.452	1.2	1782.652	235.962	433.719	106.452
OJA15	20110526	330213.996	3933016.52	1780.866	1.322	1782.188	343.996	444.52	105.866
OJA16	20110526	330305.628	3932996.14	1783.486	1.42	1784.906	435.628	424.137	108.486
OJA17	20110526	330370.076	3932902.66	1786.837	1.403	1788.24	500.076	330.664	111.837

1.2 Digital Imagery Acquisition

Two sets of digital photographic images were acquired over the course of this project; set 1 in June 2011 and set 2 in June 2013. Both image sets were collected under uniform, diffuse lighting conditions (i.e. overcast days) taking advantage of decreased dynamic range. This decreases any false edges or specular reflections that may arise from shadows and bright areas. Set 1 was collected in Nikon RAW + JPG; the JPGs were used as proxies. Set 2 was collected in Nikon RAW only and proxies were generated from these. Set 1 consisted of photomosaics collected from the 17 lidar scanner positions (Figure B2) and used in creating the photorealistic DOM. Set 1 was shot using a tripod for stability and with focus set to infinity in an attempt to keep camera conditions uniform with scene range varying from approximately 20 m to over 300 m. Multiple images were captured at each station to ensure more than adequate coverage, with a total of 234 images captured across the site.

Set 2 images, used for the Interpreted DOM, were collected at arbitrary locations around the amphitheater rim with the goal of large overlap and perpendicular views, although given the rugosity of this outcrop that was not always possible. Set 2 images adhere to a color managed workflow, a color normalization scheme specific to the camera and conditions under which the scene is acquired ensuring sharp, low noise imagery with uniform exposure and

color values. The camera's exposure was manually set via spot metering an 18% gray card reading with card perpendicular to the lens and ~ 45° to the sun, the strongest light source. Based on readings from the gray card ISO was kept low at 200 to retain image detail, aperture/f-stop at 13 and shutter speed of 320. The white balance was also set manually using X-Rite ColorChecker Passport white balance target (Figure B3) using the same orientation as the gray card. A reference image, to be used during processing for color normalization, was taken using the ColorChecker's 24-patch target, again oriented perpendicular to the lens and ~ 45° to the light source, i.e. sun. As the days stayed overcast, providing uniform, diffuse lighting conditions, exposure and white balance were set only once.

Figure B3. X-Rite ColorChecker Passport reference image used during color calibration and for setting the white balance in Set 2 Imagery

1.3 Lidar Data Processing

Name	Version	Citation
Innovmetric PolyWorks	v. 11.0.36	Innovmetric Software, Inc
Poisson Surface Reconstruction	v. 6.13	Kazhdan & Bolitho, 2006
Blender	v. 2.50alpha - v. 2.73	Blender.org
OpenEXR	v. 2.0	openexr.com
Agisoft PhotoScan	v. 0.9.1	Agisoft PhotoScan
ESRI ArcGIS	v. 9.3 - 10.1	ESRI, Inc.
Erdas IMAGINE	v. 11.0.1 - .0.4	Intergraph.com
GRASS GIS	v. 6.4.4.	grass.osgeo.org
impala		Straubhaar, et. al, 2011

Table B2. Software version and citation information

1.3.1 Parsing

The collected lidar data were downloaded from the scanner and preprocessed with the ILRIS-3D Parser. The parser outputs scan files in parametric image format, .pf, as a 3D digitized data set suitable for future processing steps.

1.3.2 Point Cloud Alignment

Alignment of the scans was completed in PolyWorks/IMAlign module. A Huge Translation (Table B1) allows a data set to be converted from local to global coordinate systems (and vice versa), avoiding mixing small and large numbers that may cause a loss in accuracy. Since data were collected in UTM coordinates, a large number coordinate system necessitating the Huge Translation to a small-number coordinate system in line with the software limitations of seven digits.

Data at each of the seventeen scanner positions were collected with a unique, Local Data Coordinate System (LDCS) particular to that station with point of origin, 0,0,0 located within the scanner. Upon importing the unorganized point cloud into IMAlign, units were set to meters; and as Optech is a supported digitizer in PolyWorks/IMAlign system, the remaining parameters were set to the recommended values, interpolation step at automatic, maximum angle at 85°, and maximum edge length automatic. These import settings affect mesh creation at a later point in the workflow, so choosing the right settings is important.

First, individual subgroups, from use of the pan/tilt base, were aligned within scanner positions at OJA01, OJA02, OJA05, OJA07, OJA08, OJA09, OJA10, OJA12, OJA15, OJA16, and OJA17 using an iterative best fit algorithm. The LDCS, like subgroups, is particular to a scanner position; therefore subgroups share a point of origin and possibly other tie points, thus manual intervention was not necessary for this alignment step. Once tasks were aligned, the seventeen scanner stations needed to be placed in the same coordinate space and correctly aligned with each other. This was an iterative procedure with no constraints on any of the six degrees of movement in the beginning. I began by aligning smaller scans to one larger scan using a manual point matching technique followed by the best-fit algorithm in PolyWorks/IMAlign module.

Once scans were located in the correct space, they were grouped together and the process began anew with another scan position. When all the scans were close to the correct location, constraints were activated upon the reference points, i.e. LDCS points of origin, first at 5 m, decreasing by 1 m steps until alignment was complete, resulting in the final alignment matrices (Figure B4) and a complete, correct alignment. The aligned, unorganized point cloud of 40,676,181 points was exported as a single, unorganized ASCII text file containing points and their vectors.

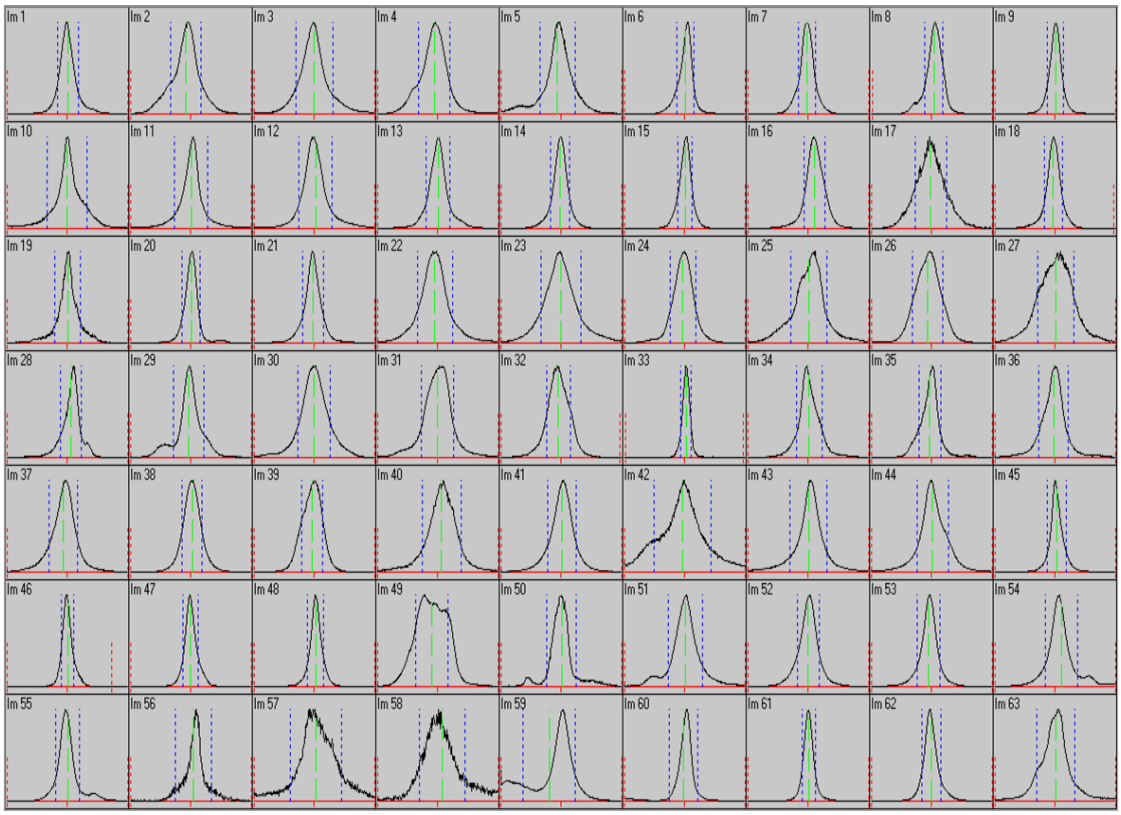

Figure B4. Image alignment error histograms for the final alignment matrices, mean and standard deviation are indicated by green and dotted lines, respectively

1.3.3 Point Cloud Editing

The text file was imported into PolyWorks/IMSurvey for cleaning and meshing. IMSurvey standard point cloud editing and processing tools were used to classify all points as either outcrop or non-face points, clipping to the just the outcrop area. Further editing included sub-sampling the uneven density of the point cloud for a uniform density. The fully edited point cloud was again exported as an unorganized point cloud of 14,293,247points in the form of a space separated, ASCII text file of x, y, z with normal vectors.

1.3.4 Mesh Construction and Editing

We then applied a Poisson Surface Reconstruction (PSR), PoissonRecon (Kazhdan, et al, 2006), via an IMEdit macro, to create a multiscale, "watertight" mesh from the point cloud (see figure 5). The PSR algorithm is global, using all points to create a smooth surface while maintaining integrity to a rugose outcrop surface with locally fitting functions (Kazhdan, et al, 2006). The PoissonRecon IMEdit macro has three parameters for mesh creation; octree depth, solver divide, and samples per node. Octree depth is the most important as a control on mesh resolution with greater depths corresponding to higher resolutions. However, this must be countered by the available RAM and overall size of the point cloud. The mesh was generated using an octree depth of 14 on a computer with 24 GB of RAM and a point cloud with just over fourteen million points. Solver divide, second PSR parameter, controls splitting the reconstruction into

multiple processes to avoid overworking available RAM, I found a solver divide of 10 to work well. The third parameter specifies minimum number of points that must be in an octree node, considering the point cloud had been subsampled for uniformity, two samples per node worked well. This created a "watertight" mesh, or completely closed volume with false connections between real gaps in the outcrop (Figure B5).

The resulting mesh was edited with standard IMEdit tools. First, I selected and deleted all triangles with an edge length greater than 0.75 m since the triangles in unsampled areas were very large (Figure B5). This step cleaned most of the false connections. The mesh also contained some disconnected "blob" artifacts resulting from trees and bushes at the outcrop base. These blobs or shells contain a very small number of triangles, and as such are easy to select and remove.

The mesh was useable at this point but very dense, such that additional editing was required. Close vertices were merged and the number of faces reduced with IMCompress. A check was done to find and delete intersecting faces. Any holes resulting from this step were then filled. To verify multiple surfaces were not created during the meshing process, the mesh was imported back into IMSurvey and cross sections were cut every 20 m in both x and y planes.

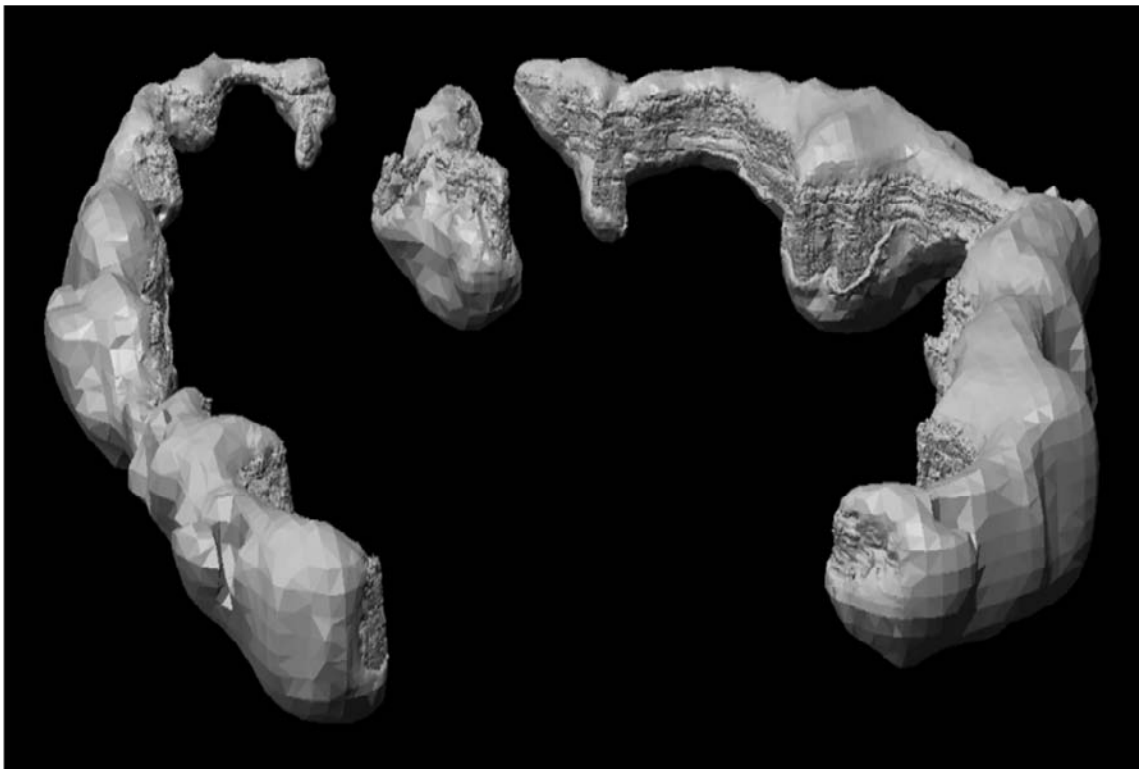

Figure B5. Oblique easterly view of Ojito Amphitheater showing watertight mesh effect of PSR and large triangle edge length in unsampled areas

The final editing step, in IMEdit, improved edge depiction and surface curvature with the Optimize Mesh command. Default parameters were used: 1° sensitivity between the concavity of a triangle pair, minimum of 4 triangles/vertex, maximum of 10, 15° minimum inner angle, and 45° maximum dihedral angle. A check in IMSurvey showed the average edge length to be 9.124 cm, with 28,567,297 triangles. Spatial errors from the mesh vertices to corresponding point cloud points are millimeter to centimeter scale, Fig. B6. The edited mesh was exported as a .ply for unwrapping in Blender.

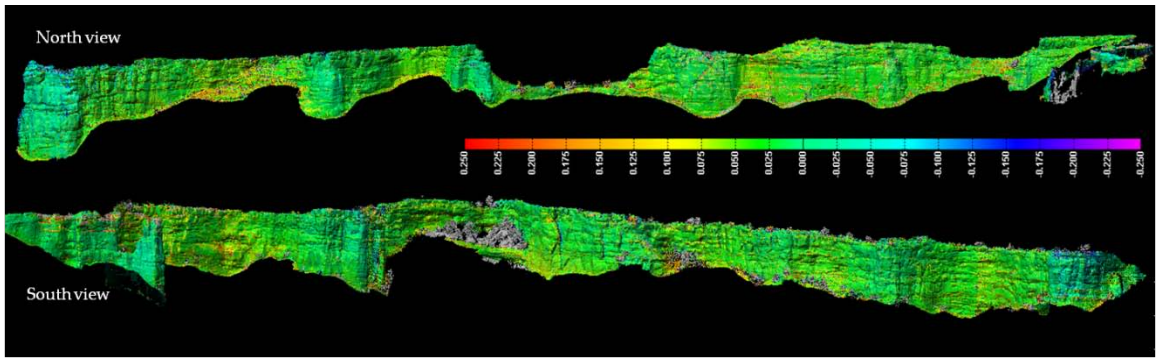

Figure B6. Error map displaying spatial difference between mesh vertices and corresponding point cloud points, scale is in meters

1.3.5 Mesh Unwrapping

Prior to unwrapping the meshes, two steps were done to improve results. First, the mesh was divided into twelve sections to bring the number of faces in an individual section down to a more manageable number. Second, planar and nearly planar triangular faces were converted to quads for further reduction and smoothing. Quads are polygons with four sides and four vertices, this allows for a more balanced division, i.e. four divided by two as opposed to three divided by two.

UV mapping is the process of mapping (projecting) a 2D texture over a 3D object. Before a texture, either photograph or interpreted image, can be projected onto a mesh, the 3D mesh must be converted to 2D, a process known as unwrapping. The UV terminology is used to refer to "texture-space coordinates" instead of x, y, z "3D space"; it is a process of assigning 2D coordinates to the vertices. Similar to cutting a paper model of an object in specific places so that it

can lay flat, the twelve meshes can be cut to be transformed into a representative 2D system (Figure B7). Each point in the UV map correlates to a vertex in the mesh, UV map lines are mesh edges and UV map faces are mesh faces. Blender, an open source 3D computer graphics software, currently has the best tool for unwrapping complicated, dense meshes with their Smart UV Project tool. An 8,000-pixel resolution image was created for Blender to assign the UV map to designated .png for lossless compression. The Smart UV Project splits the mesh into islands, or groups, based on angular changes in the mesh and three user-defined parameters. Angle limit, the first parameter, controls how faces are grouped and refers to the angle between faces; a higher limit results in many small islands with low distortion, lower limits the opposite. I chose a high angle limit of 80 because my meshes were dense and I wanted to lessen distortion. Next, island margin, controls distance between islands, space that allows texture to "bleed" beyond one island without painting another. This parameter is difficult to set as Blender calculates margins as float parameters relative to the size of each island (http://wiki.blender.org/index.php/User:Shuvro/soc2011), therefore making it impossible to achieve uniform margins. I set the parameter to 0.01, with margins from 0.005 to 0.01 reasonable. As part of the procedure, each island is projected onto a plane; the resultant normal of that plane is an average of all the faces normal vectors. Area weight, the third parameter,

controls how much each face's normal is weighted based on the area it occupies in the island; however, I used an area weight of zero, voiding this parameter. Once the UV mapping image is created and these parameters set, unwrapping can be done.

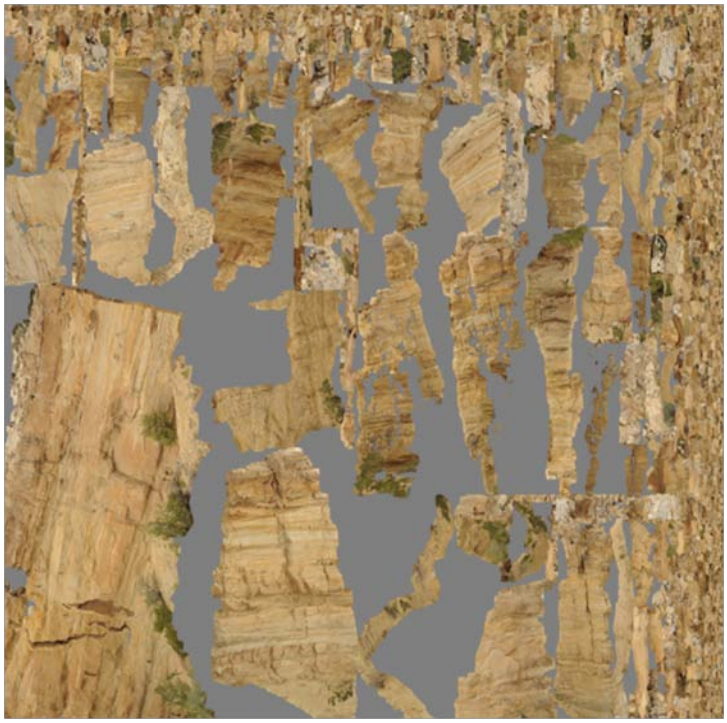

Figure B7. Unwrapped mesh

1.4 Digital Imagery Processing

The Photorealistic DOM is a collection of measurements of an outcrop's geometry and surface properties. The terrestrial lidar derived mesh serves to measure scene geometry, while surface properties are captured with digital photography. This section details building the Photorealistic DOM by first calibrating the camera, rectifying set 1 imagery and projecting this undistorted

imagery onto the terrestrial lidar derived mesh. This section also covers calibration and rectification of set 2 imagery.

1.4.1 Camera Calibration and Image Rectification

1.4.1.1 Set 1 Imagery

Before any of the images can be projected onto the mesh, the camera must be calibrated in order to find internal distortion parameters and external parameters describing poses when images were captured. Internal distortion parameters are comprised of both radial distortion, a result of the lens shape, and tangential distortion, a result of the camera's assembly process. External parameters describe the pose of an object relative to the camera and can be defined in terms of rotation, describing a point's location in a new coordinate system, and the translation vector, shifting the origin to the new coordinate system (Bradski and Kaehler 2008).

For the Photorealistic DOM, using set 1 imagery, calibration was completed with Cam-Rx manually using OpenCV algorithms (Bradski and Kaehler, 2008) based on a pinhole camera model where 3D points are projected onto the image plane with a perspective transformation (http://docs.opencv.org/modules/calib3d/doc/camera_calibration_and_3d_reconstruction.html). Cam-Rx (Figure B8) a GUI to the OpenCV camera calibration functions, was used in conjunction with IMSurvey to manually digitize tie

points, between the 2D image and 3D mesh, and solve for external, or pose, parameters. Cam-Rx utilizes RANSAC, a random sample consensus, iterative, optimization algorithm to solve for each pose. Even though the statistics do differ from image to image, some generalizations were true; each image contained at minimum ten tie points and overall RMS was always within two pixels. Thirty-four images were required to cover scene geometry of the entire amphitheater. Cam-Rx outputs an undistorted jpeg image, camera pose matrix, 3D object coordinates and matching 2D image coordinates for each tie point.

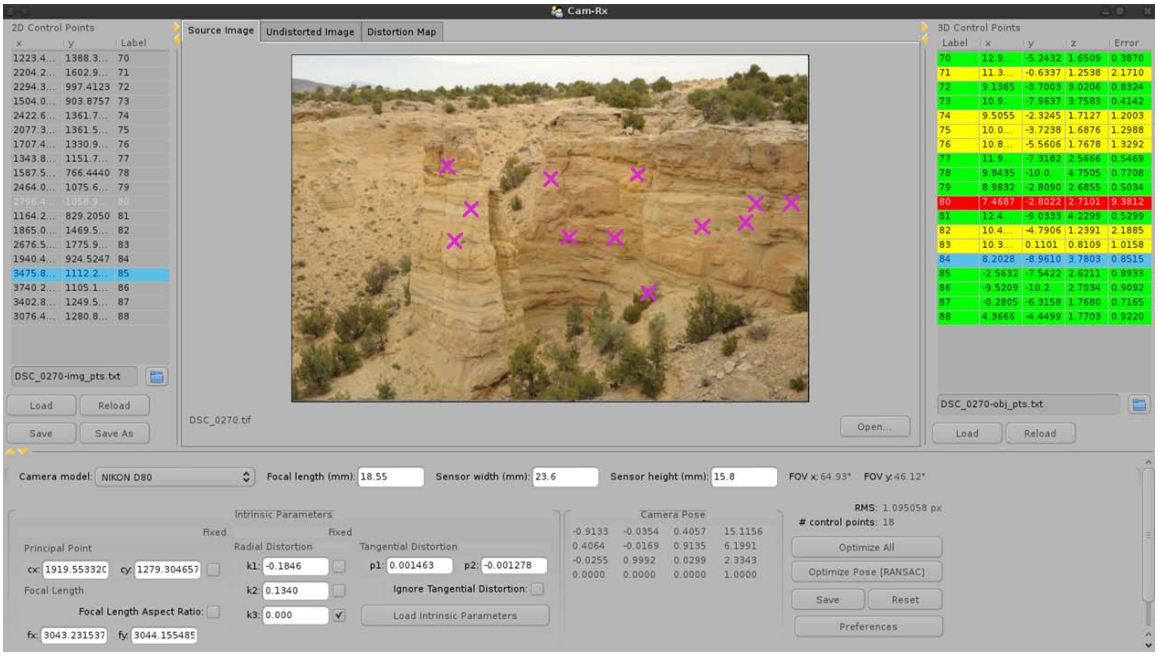

Figure B8. Cam-Rx interface

1.4.1.2 Set 2 Imagery

A portion of the work focused on refining data collection and analysis procedures to improve accuracy and reliability of interpretations, which is the reasoning behind set 2 imagery. By moving to a calibration procedure based

on dense stereo matching, as found in Agisoft PhotoScan , we were able to increase the maximum number of photographs handled by at least an order of magnitude, from a few dozen to 445. The new approach strengthened calibration results and increased resolution of the Interpreted DOM.

To make the most out of PhotoScan, imagery was transformed from raw format to a scene linear 16-bit floating point OpenEXR format, a high-dynamic-range image file format that allows for better color precision and measurement. Depth Filtering, in PhotoScan's preference settings, was set to mild, recommended for a complex surface. Using the alignment workflow in PhotoScan, set 2 images were loaded and inspected; some images were removed due to prior modification of image size, i.e. turning the camera 90°. Pair preselection was disabled as images were not always captured continuously. Accuracy was first set lower, and then adjusted higher once camera poses were roughly approximated. Due to the complexity of this outcrop, masks were created in Blender to obscure all but the outcrop face for all images and imported to constrain feature detection to just the outcrop face. In addition, tie points were manually placed on images to aid in the alignment process. These tie points also served as 3D ground control points for transforming the coordinate system from arbitrary, local system to 3D, real world coordinate system used by IMSurvey. Once calibration parameters were calculated, the scene geometry was

reconstructed. The resultant texture has an average resolution of 0.0615 m/pixel and an average point density of 52,360 points/m^2. PhotoScan alignment resulted in a stronger calibration than with Cam-Rx, due to the number of images and tie points used; however, it is difficult to compare the two calibration procedures since they have very different results.

The color managed workflow (see B 1.2 Digital Imagery Acquisition) was applied so image segmentation could be performed on images with higher color resolution and a more direct, quantifiable relationship to the scene's physical properties. Set 2 imagery adheres to this workflow, where we attempted to calibrate for color in order to quantify the values. To measure color based on the scene's physical properties, images were processed in RAW development using raw2cs, a python script that employs three tools; dcraw transforms raw data to a linear color space, oiiotool normalizes data, and exiftool for metadata manipulation. We processed the reference image (Figure B3) to a 16-bit scene-referred linear tiff from raw using raw2cs to measure color values captured by the Nikon D700 under those day's specific conditions. The measured values were then used to normalize color space such that the 18% gray card measured 0.18 and complete white measured 1.0 with the oiiotool. The normalization was applied to all set 2 imagery.

1.4.2 Texture Mapping

Once set 1 images were rectified for distortion, they were projected onto the mesh, completing the Photorealistic DOM. Projecting or texture mapping, is a continuation of UV unwrapping in Blender, detailed in section 1.3.5 Mesh Unwrapping above. The individual camera poses from Cam-Rx were imported into Blender and the undistorted images painted on the UV map. Using the Texture Paint mode in Blender, the clone brush was used, brush strength set to 1 for imagery being applied in full, 0 for blended images. The bleed parameter allows texture to bleed into the island margins with settings from 1 to 5, roughly a percentage of the available space with 5 corresponding to the entire margin; I used a bleed of 2 or 3 depending on the mesh. Some images were applied in full, while others were applied with more care using a graphics tablet. After mapping, the DOM was exported as .obj, a text file with UV coordinates, and associated .mtl, the materials file for import into PolyWorks IMSurvey as a polygonal model. PolyWorks is limited in displaying only JPEG textures; therefore an additional step is to change the file format in the .mtl file from .png to .jpg. At this point, the photorealistic DOM was complete with measureable surface properties and geometries (Figure B9).

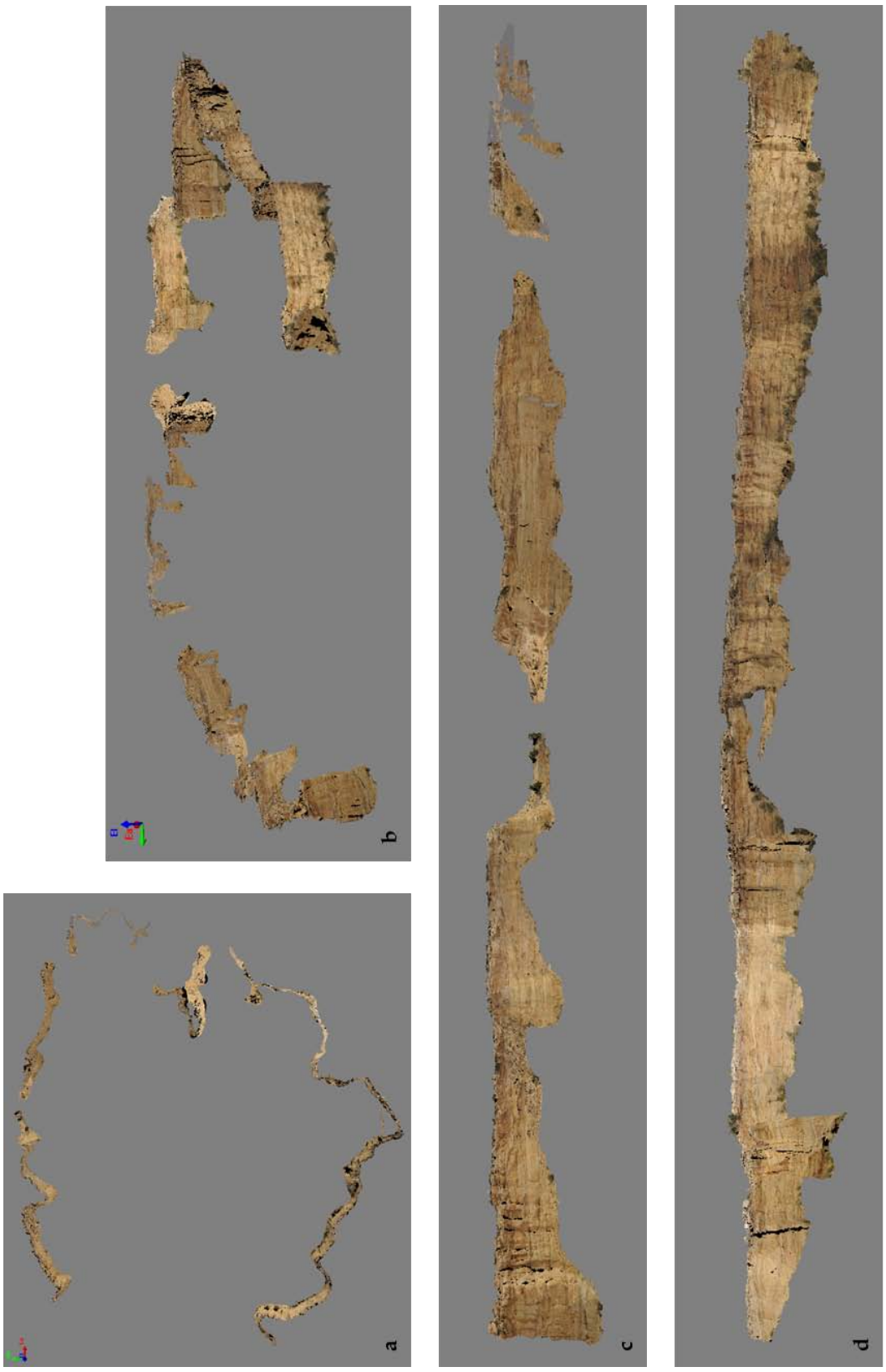

Figure B9. Photorealistic DOM. a) Map view b) oblique easterly view c) north side of the amphitheater d) south side of the amphitheater

2 Architectural Element Analyses and Classification

Architectural element analysis provides the foundation for classification at this outcrop. Again, the reader will find similarities between Ch. 2 and this section of the Appendix; however, more detail is reported here, including some work that was not ultimately used. Section 2.2 5th Order Bounding Surfaces is reported on as this work has potential for use if one were to approach MPS hierarchically in a manner similar to that of Weissmann and Fogg (1999). These surfaces can be used as a framework dividing the outcrop into sections and creating separate TIs in each one.

2.1 Architectural Element Analysis

Architectural element analysis (Miall, 1985), a lateral profiling technique, is often applied to understand the distributions of fluvial facies on an outcrop. In addition, fluvial bounding surfaces provide a framework for integrating geologic information into stochastic models and some large-scale mapping and analysis suggests fourth order bounding surfaces correspond to large-scale permeability correlation structures (Davis et al. 1997). In the case of Westwater Canyon, architecture of sandstone bodies controls fluid flow and subsequent uranium emplacement (Cowan 1992). The subset outcrop (Figure B2) (see Ch. 2 Building a Better Training Image with Digital Outcrop Models, 2.3 Site Description for the explanation) was studied according to field methodology proposed by Miall

(1985), with some allowances for technological advances. Digital images were taken of the outcrop, the position approximately normal to the face being photographed. While in the field, major bounding surfaces and minor elements were traced on print copies of the digital images. In places where the outcrop was unreachable, binoculars were used. Information was digitized onto photographs and analyzed in ArcGIS and IMSurvey.

The digitized images are shown in Figure B10, from north to south respectively, with details listed in Tables B3, B4 and B5. Six major depositional units, labeled A – F, separated by 5th order bounding surfaces, were identified. Unit A, the lowest, is visible over a just a very small area and is composed of distinctly laminated fine sand (Fl) with the lower bounding surface hidden underground; therefore, Unit A is not included in Ch. 2, but is reported on here, briefly, for the sake of completeness. The lower boundaries of units B - F are delineated by a relatively coarser facies containing clay clast conglomerates (Figure B11). These 5th order bounding surfaces separate the six major depositional units (A-F) and extend across the entire outcrop study area, resulting in five major depositional units correlatable across the amphitheater; B, C, D, E, and F. Units D, E, and F are laterally continuous across the entire site.

Unit B has irregular, erosional lower contact with Unit A. The exposed lateral extent of Unit B is too small for external geometry to be known. Unit B

contains the coarser, clay clast conglomerate facies heavily interbedded with fine sand, thus this is a heterolithic unit with some visible horizontal laminations (Sh), two occurrences displaying primary current lineations indicating paleoflow in both northwest/ southeast and north/south directions. Unit C's displays an overall sheet geometry across the subset study area. Internal assemblages include low angle crossbeds (Sl) inside 4th order bounded minor channels with flat to concave up bases. Some of the lithofacies (Sl and Sh) in Unit C display primary current lineations indicating either northwest or southeast paleoflow. Parts of Unit C appear to be massive (Sm). Unit D has an erosional, planar lower boundary. The external geometry is sheet. Internally Unit D contains solitary and grouped trough crossbeds (St); horizontal laminations (Sh), low angle crossbeds (Sl) and one very broad, shallow planar crossbedded scour (Sp). Unit E has an irregular, erosional lower boundary, and its external geometry appears to be tabular. Internal geometries and assemblages include multiple scours with low angle crossbeds (Sl), some of which are broad and very shallow. Horizontal laminations (Sh) are associated with the low angle crossbeds. Primary current lineations associated with some Sh lithofacies indicate northwest/southeast flow, with some trough crossbedding indicating northwest flow. Unit F has wavy erosional lower boundary and is tabular shaped with horizontal laminations (Sh)

and multiple 4th order bounded minor channel fill deposits with concave up, scoop shaped bases.

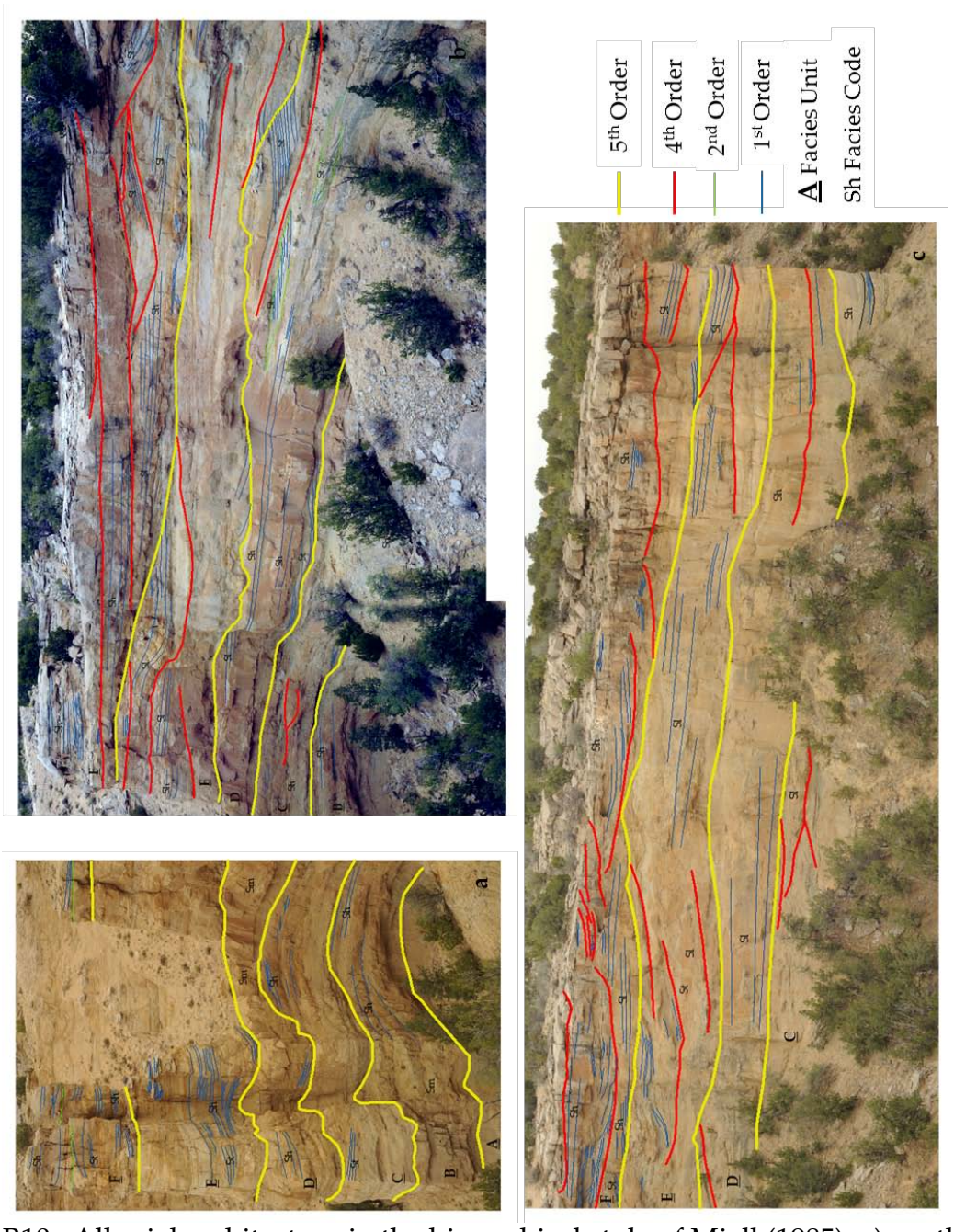

Figure B10. Alluvial architecture in the hierarchical style of Miall (1985) a) north segment of subset outcrop b) east segment of subset outcrop c) south segment of subset outcrop

For all units, except A, the massive and low angle to planar bedded facies are fine to lower medium grained sand, while the trough cross bedded facies are fine to upper medium with some coarse grains. A trend of decreasing clay clast conglomerate exists upward in the section. Paleoflow indicators, including trough crossbedding and primary current lineations, vary widely from northwest/southeast to north/south to northeast/southwest. This dispersion could be the result of localized flow concentration around bars.

Facies Code	Facies	Sedimentary Structures	Interpretation
St	Sand, fine to v coarse, may be pebbly	Solitary, or grouped, trough crossbeds	Sinuous-crested and linguoid 3D dunes
Sp	Sand, fine to v coarse, may be pebbly	Solitary, or grouped, planar crossbeds	Transverse and linguoid bedforms 2D dunes
Sh	Sand, v fine to v coarse, may be pebbly	Horizontal lamination parting or streaming lineation	Plane-bed flow (critical flow)
Sl	Sand, v fine to v coarse, may be pebbly	Low angle crossbeds	Scour fills, humpback or washed-out dunes
Sm	Sand, fine to coarse	Massive, or faint lamination	Sediment gravity flow deposits
Fl	Sand, Silt, Mud	Fine lamination, very small ripples	Overbank, abandoned channel, waning flood deposits

Table B3. Facies classification. Modified from Miall (1996)

Rank	Fluvial Depositional Unit	Bounding Surface Characteristics and Geometries
1	Ripple	Sheet, wedge, lens
2	Dune	Coset Bounding Surface, sheet, wedge, lens
3	Macroform Growth Increment	Wedge with flat base, dipping 5-20° in direction of accretion
4	Macroform, Point Bar, Minor Channel Scour	Wedge, lens with flat base and convex up upper depositional surface
5	Channel	Flat to concave up channel base, sheet, ribbon

Table B4. Hierarchy of depositional units and bounding surfaces. Modified from Miall (1996)

Element	Symbol	Principle Lithofacies Assemblage	Geometry and Relationships
Channels	CH	Any	Finger, lens, sheet, concave up erosional base, scale and shape highly variable
Sandy Bedforms	SB	St Sp Sh Sl	Lens, sheet, blanket, wedge, occurs as channel fills, crevasse splays
Lateral Accretion Deposits	LA	St Sp Sh Sl	Wedge, sheet, lobe, characterized by internal lateral accretion surfaces
Laminated Sand Sheets	LS	Sh Sl minor St Sp	Sheet, blanket
Overbank Fines	OF	Fm Fl	Thin to thick blankets, commonly interbedded with SB

Table B5. Architectural elements in fluvial deposits. Modified from Miall (1985)

Figure B11. Coarser facies containing clay clast conglomerate that commonly delineates the lower boundaries for units B – F

Of the 6 units, 4 are interpreted as being composed of amalgamated channel belt deposits (B, C, E, and F). The internal structure observed in these units are mostly low angle crossbeds (Sl) and horizontally laminated (Sh). These facies are often associated with each other and indicate upper flow regime or a transition from subcritical to supercritical status (Miall 1996) and could be indicative of flashy seasonal flow conditions, i.e. monsoonal, at the time of deposition (e.g. Fielding et al. 2009; Plink-Björklund 2015). In modern analogs, these can be stable bedforms in fine to medium sands at depths between 0.25 m and 0.5 m. Unit B, although not exposed across the site, does display low angle crossbeds

(Sl) downlapping on horizontal laminae (Sh), capturing a depositional moment where the bedform is approaching supercritical flow and upper flow regime.

Unit A's depositional environment is interpreted as overland flow (OF), i.e. an abandoned channel or flood plain, based on composition. Unit A is most likely an abandoned channel as no paleosols or root traces were evident. The distinct laminations (Fl) are due to suspension settling.

Unit D consists primarily of laminated sands (LS), commonly interpreted as upper flow regime flash flood deposits (Miall 1985; Fielding et al. 2009). These sand sheets are topped by trough crossbeds deposited at the end of flood conditions when discharge and velocity decrease; the horizontal laminae are capped with facies St. The many 4th order minor channels with concave up bases similar to those observed in Unit D have been described in other areas of Westwater Canyon, and a new depositional environment created, Hollow Element, HO, concave-up troughs filled with inclined parallel to low angle crossbedding (Godin 1991). This element is interpreted as short-lived scours at convergence points (Cowan 1991; Godin 1991; Miall 1996).

2.2 Interpolation of the 5th Order Bounding Surfaces

The 5th order major boundaries were digitized in PolyWorks IMSurvey on the DOM. IMSurvey allows the user to create features, called primitives, and attach the newly created primitive to another, existing data object. Under the

Create Features menu, I chose polyline, and then the Pick then Fit sub-method so to anchor the bounding surface polylines directly to DOM vertices. The polyline vertices were subsampled to 50 cm for a more even density along the lines and the fit was visually verified at random areas. 5th order lower bounding surface polylines were digitized for units C, D, E, and F. Unit B was not included as the lower bounding surface area was not exposed as extensively as the other units. The polylines were exported as x, y, z text files.

The digitized bounding surface polylines were then imported into ArcGIS for interpolation across the amphitheater in order to construct a 3D model of bounding surface distribution for a general physical geologic framework. Universal kriging was used to interpolate surfaces, as the global trend, a slight northwest dip needed to be removed. The Geostatistical Wizard, a part of the Geostatistical Analyst extension in ArcGIS, was used, and the surfaces can be seen in Figure B12. The surfaces, once interpolated, were then exported for use with the DOM in both PolyWorks IMSurvey and Blender.

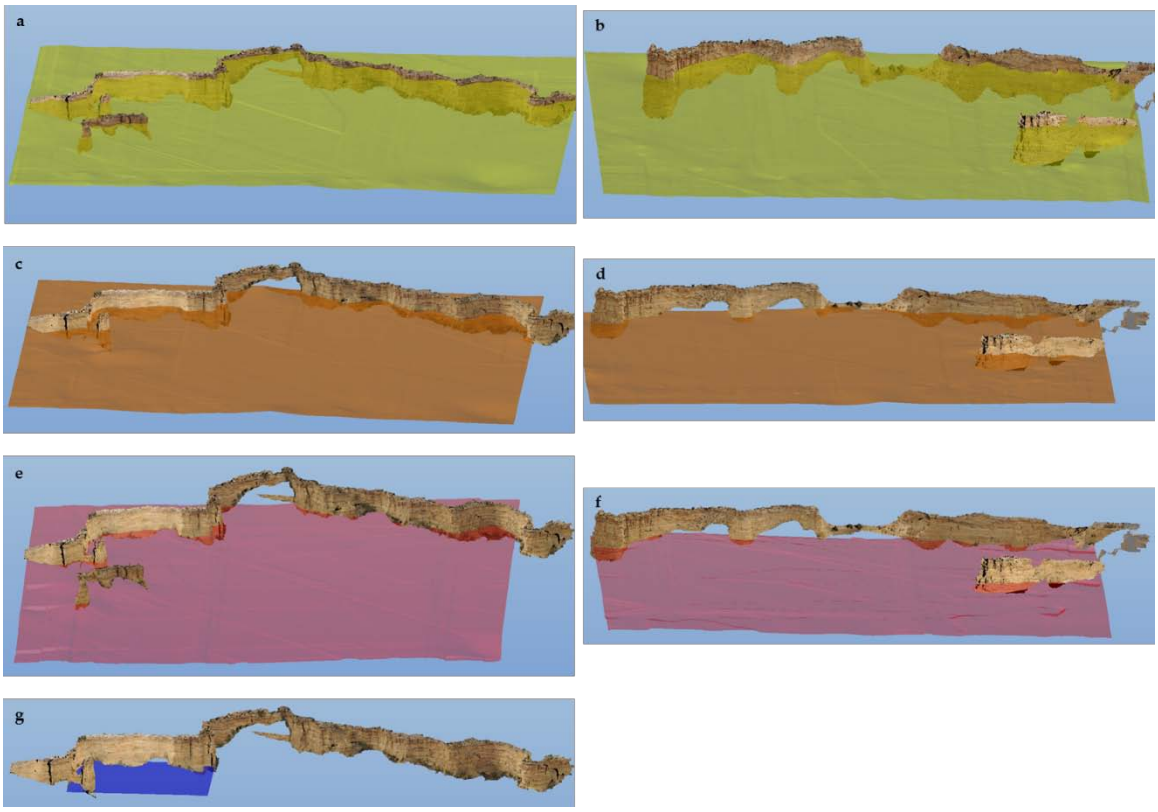

Figure B12. Planes interpolated from 5th Order Bounding Surfaces a) F surface, south view b) F surface, north view c) E surface, south view d) E surface, north view e) D surface, south view f) D surface, north view g) C surface, south view

2.3 Hydrofacies Classification

Based on architectural element geometries and grain size characteristics, facies in the subset amphitheater area were classified into four hydrofacies; fines/clays, fine to lower medium massively bedded sands, fine to lower medium low angle sands, and fine to upper medium trough cross-bedded sands with some coarse grains. Traditional photogrammetric classification and feature extraction approaches were employed. The following steps were completed using ERDAS Imagine. Planar, low angle and trough cross-bedding sedimentary features were highlighted and extracted with diagonal (Figure B13b) and

horizontal zero-sum edge detection filters (Figure B13c) available under the Spatial Enhancement menu for image interpretation. Zero-sum filters are a special class of convolution filters operating in the spatial domain of the image, which work by averaging small sets of pixels across the entire image (Jensen, 1996).

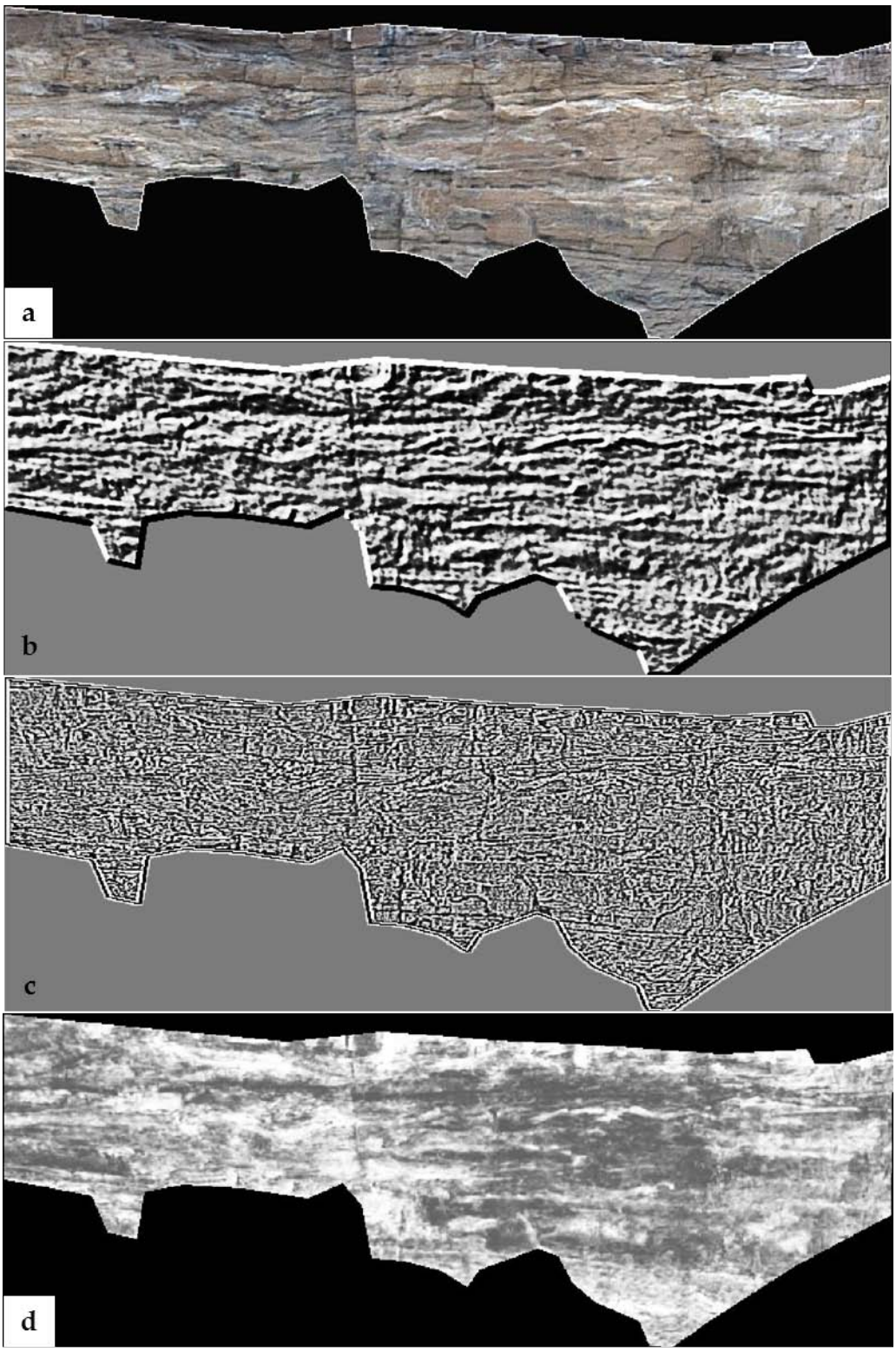

Figure B13. a) RGB image of outcrop face b) 5x5 diagonal edge detection c) 3x3 horizontal edge detection d) index emphasizing blue/green colors

Color indices are commonly used for feature extraction in geology; here they were used to distinguish the more blue clay clast conglomerates areas from surrounding red and tan sandstones (Figure B13d). The index, described in Figure B14, was applied to each pixel in the image.

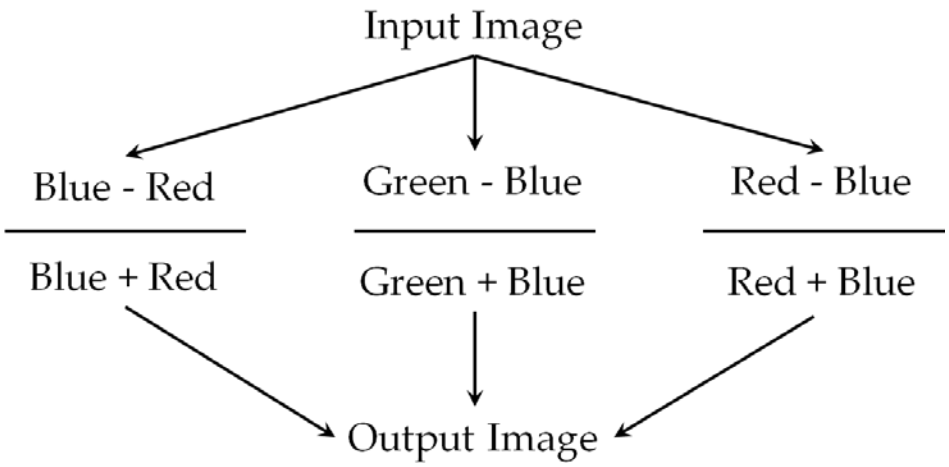

Figure B13. Schematic of the color index applied to enhance the more blue clay rich areas over the red and yellow sandstones

Classification was manually digitized onto set 2 rectified images (Figure B15a) and then projected onto the mesh using the same techniques as with set 1 (see B 1.4.2 Texture Mapping, this document), to complete the interpreted DOM, Figure B15b. The data were exported from PolyWorks IMSurvey in x y z + RGB form as an ASCII text file.

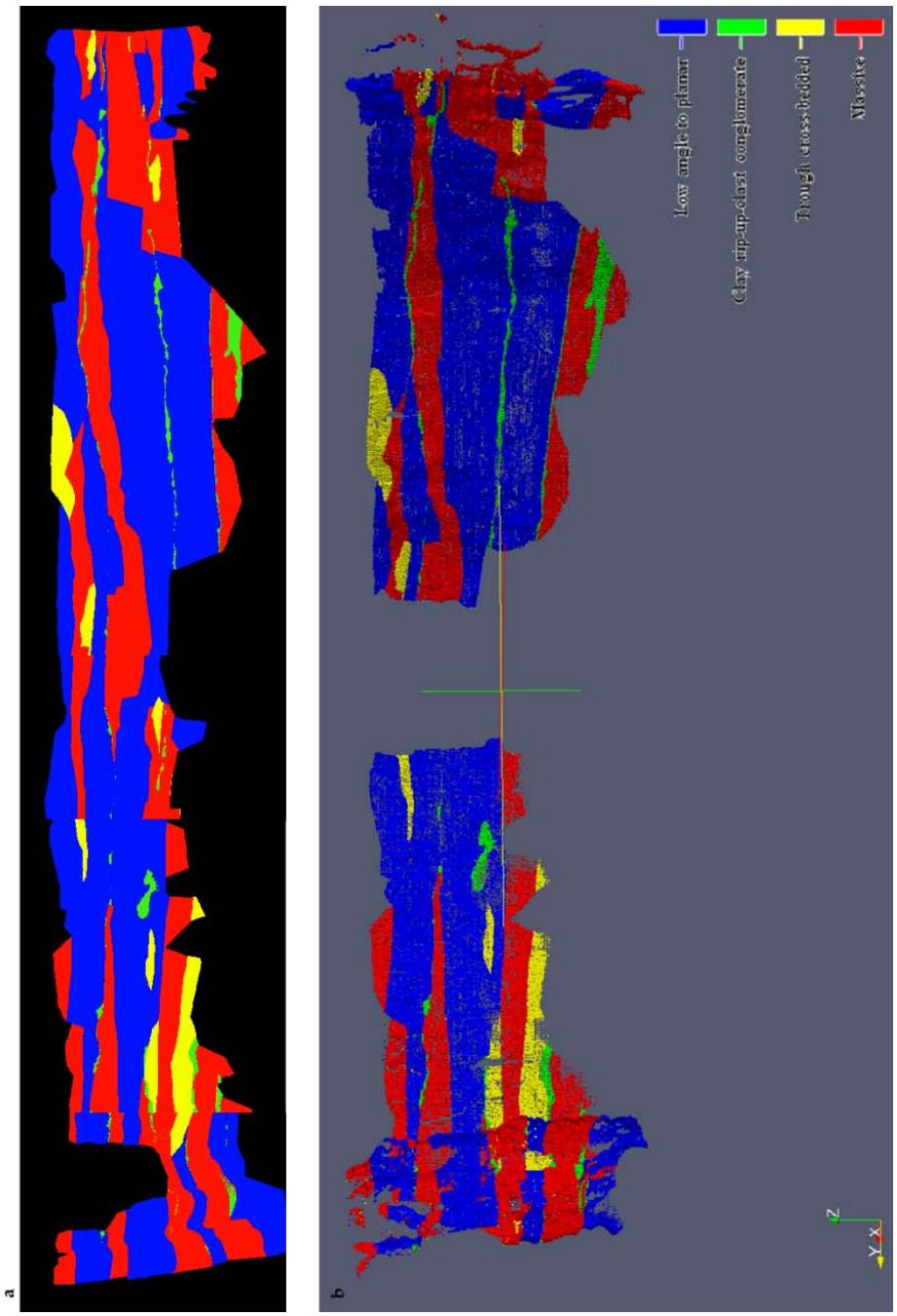

Figure B15. a) Fully classified photo mosaic of subset outcrop b) southeasterly view of interpreted DOM

.

3 Training Image Generation and MPS realization

In this work, two approaches were tested to tackle the lack of a full 3D training image (Figure B1). The first approach, Impala, considered the outcrop as a 3D training image containing some missing data; this approach was not presented in Ch. 2 because the resulting realizations appeared to be noisy. The second option, s2Dcd + Impala, is reported on in Ch. 2 and, again the reader may notice some similarities between the two sections.

The interpreted DOM data were discretized on a 10 cm structured grid in GRASS GIS with the g.region module, then imported using GRASS' r3.in.xyz tool, which imports xyz data from an ASCII text file into a 3D raster map of voxels (3D pixels, or pixels that have volume). Areas of the image containing no data were flagged -1 as the region created was a rectangular volume. Once imported, the dataset was exported in vtk format, consistent with use in *impala* using GRASS GIS' r3.out.vtk module, for outputting 3D raster maps into vtk-ASCII format. The MPS simulation engine adopted in this work (*impala,* Straubhaar et al. 2011) allows users to handle this kind of incomplete training image. The incomplete training image (interpreted DOM dataset) was scanned as if a full 3D training image, and where no information, i.e. -1, voxels existed the dimension was reduced. This is a standard approach adopted in 3D MPS simulations where no replicates of a given data event are found in a full 3D

training image. In this case, the MPS simulation algorithm was not able to find a statistically meaningful number of data events, or perhaps the data events are too small to capture big scale structures, resulting in noisy realizations, Figure B16.

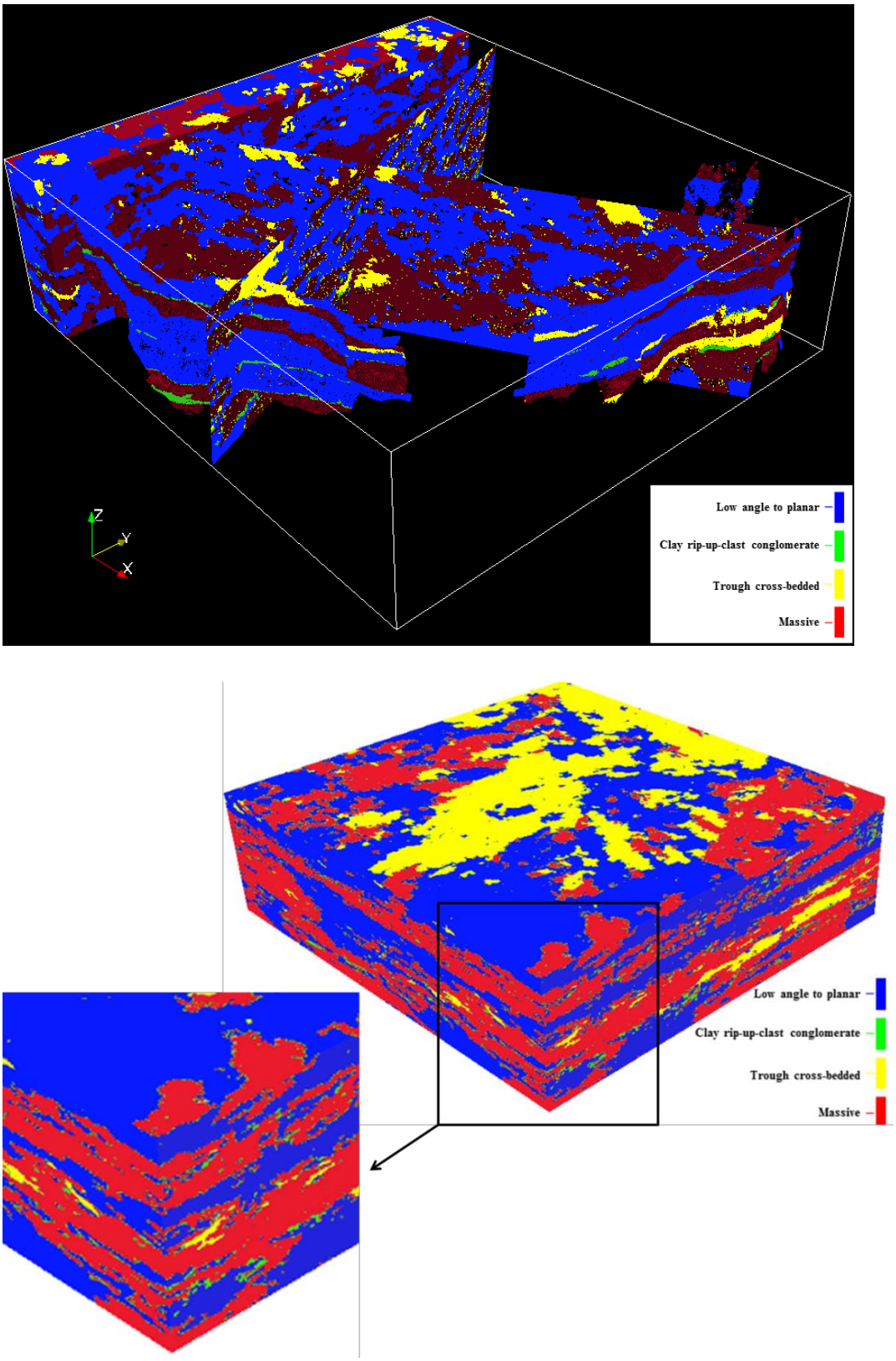

Figure B16. *impala* results from the incomplete 3D training image

For the second option, s2Dcd and *impala*, the 3D dataset was divided into two orthogonal sections (Figure B17) and projected on vertical planes approximating the outcrop shape. The sections were projected onto planes using GRASS GIS' r.in.xyz module by importing y, z in the x, y columns and x, z for x, y. The data were then exported using r.out.vtk. In the s2Dcd method, the 2D MPS simulations are performed along a given sequence using 2D training images. At each step, the facies codes simulated just prior are considered conditioning data. In this way, with a series of 2D simulations, a 3D domain is filled while preserving the overall coherence. The s2Dcd requires a MPS simulation engine, and in this study, we used the same tool as before (impala, Straubhaar et al, 2011), resulting in the realization shown in Figure B18. However, there are inconsistencies in the facies distribution of the two training images, which are further emphasized by considering the *z* coordinate as an auxiliary variable. This highlights a limiting assumption of the s2Dcd approach regarding heterogeneity symmetry in the simulation domain. One way to decrease the noise from this assumption is the use the same training image along both simulation domains, just rotated normal to itself. This approach, however, would limit the ability to reasonably model anisotropy common in fluvial successions.

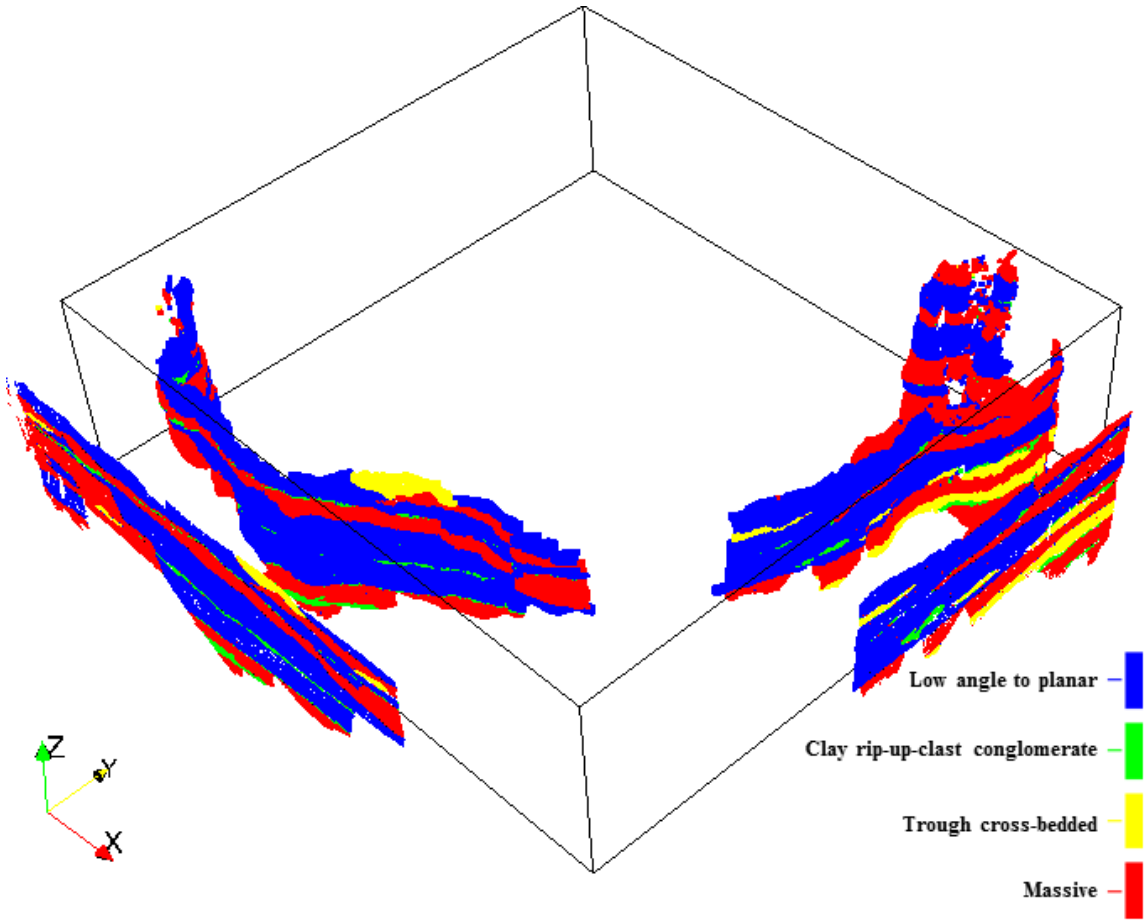

Figure B17. Projecting interpreted DOM onto 2D planes

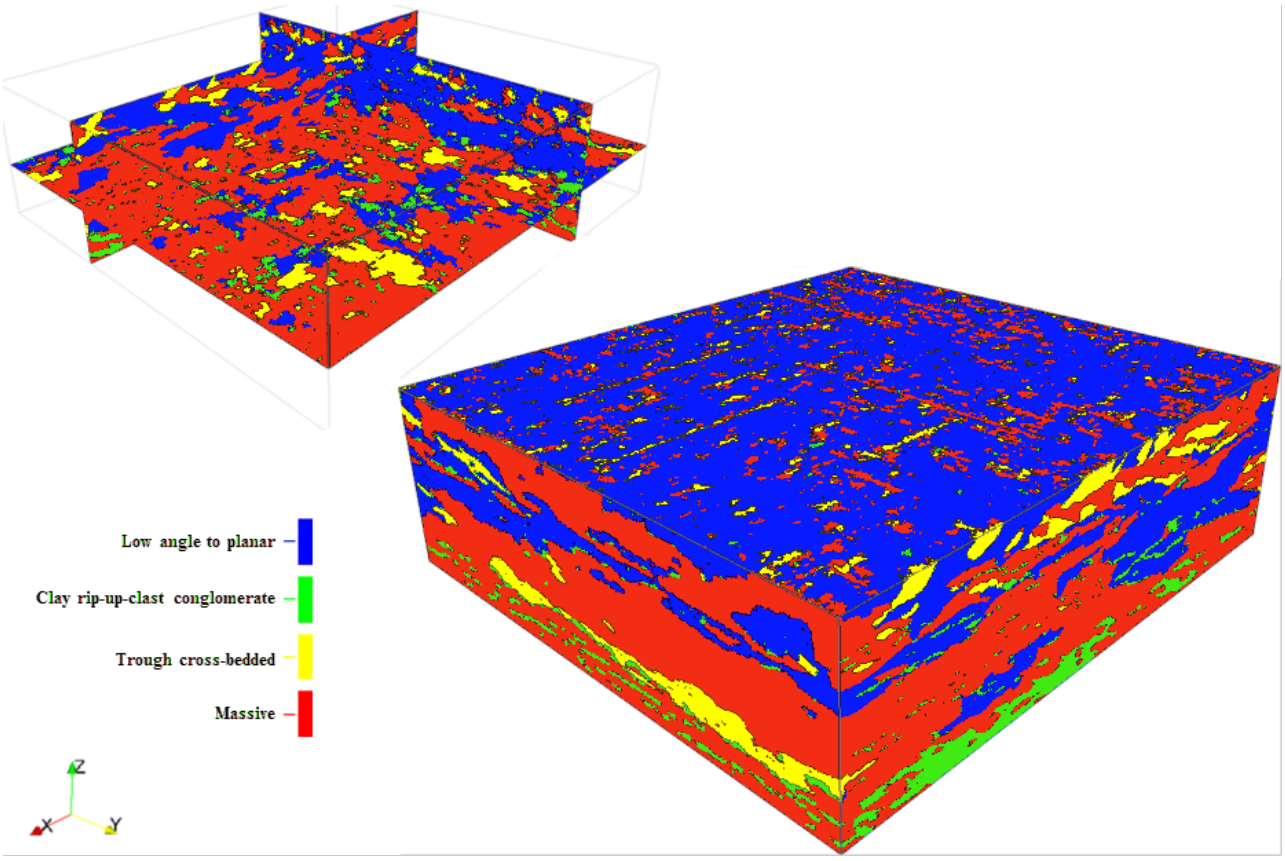

Figure B18. MPS results, s2Dcd + Impala using both training images

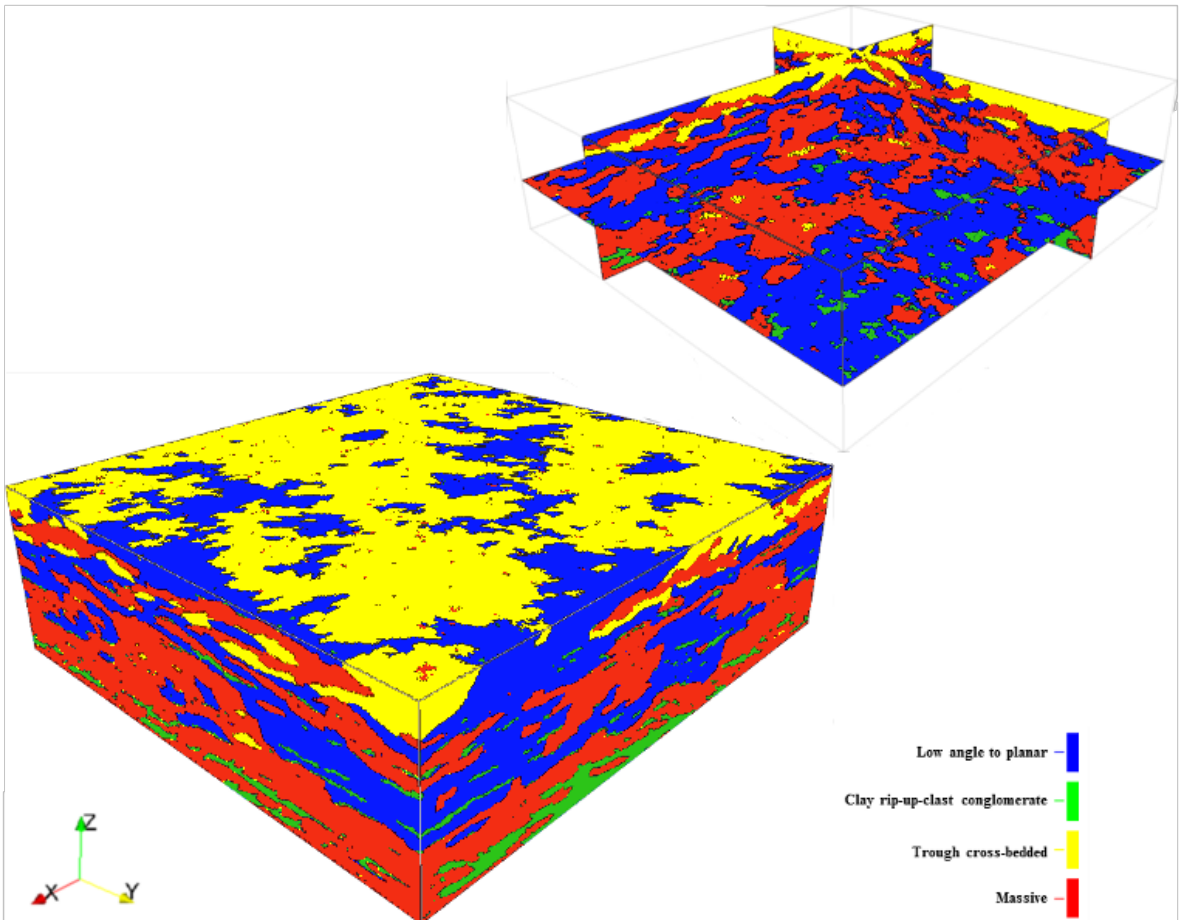

Figure B19. Results of s2Dcd + Impala MPS simulation using only 1 training image, but rotated so in both simulation directions

References

Agisoft PhotoScan, v. 0.9.1, Professional Ed.

Anderson, M.P., 1989, Hydrogeologic facies models to delineate large-scale spatial trends in glacial and gaciofluvial sediments, Geological Society of America Bulletin, v. 101, n. 4, p. 501-511, DOI: :10.1130/0016-7606(1989)101<0501:HFMTDL>2.3.CO;2.

ArcGIS, v. 9.3-10.1, ESRI, Inc.

Baldwin, J.A., & D.R. Rankin, 1995, Hydrogeology of Cibola County, New Mexico, USGS Water-Resources Investigations Report 94-4178.

Bayer, P., P. Huggenberger, P. Renard, & A. Comunian, 2011, Three-dimensional high resolution fluvio-glacial aquifer analog: Part 1: Field Study, Journal of Hydrology, vol. 405, n. 1, p. 1-9, DOI: 10.1016/j.jhydrol.2011.03.038.

Bellian, J. A., C. Kerans., & D.C. Jennette, 2005, Digital outcrop models: applications of terrestrial scanning lidar technology in stratigraphic modeling, Journal of Sedimentary Research, v. 75, n. 2, p. 166-176, DOI: 10.2110/jsr.2005.013.

Blender, v. 2.50alpha - .73, www.blender.org.

Bradski, G. & A. Kaehler, 2008, Learning OpenCV: Computer vision with the OpenCV library, O'Reilly Media, Inc.

Bridge, J.S., 2003, Rivers and Floodplains; Forms, Processes, and Sedimentary Record, Blackwell Publishing, Malden, MA, 491 p.

Boucher, A., 2011, Strategies for modeling with multiple-point simulation algorithms, Closing the gap: advances in applied geomodeling for hydrocarbon reservoirs, Canadian Society of Petroleum Geologists, Calgary, p. 67-73.

Buckley, S.J., J.A. Howell, H.D. Enge, & T.H. Kurz, 2008, Terrestrial laser scanning in geology: data acquisition, processing and accuracy considerations,

Journal of the Geological Society, London, v. 165, p. 625-638, DOI: 10.1144/0016-76492007-100.

Buckley, S.J., H.D. Enge, C. Carlsson, & J.A. Howell, 2010, Terrestrial laser scanning for use in virtual outcrop geology, The Photogrammetric Record, v. 25, n. 131, p. 225-239, DOI: 10.1111/j.1477-9730.2010.00585.x.

Burton, D., D.B. Dunlap, L.J. Wood, & P.P. Flaig, 2011, Lidar intensity as a remote sensor of rock properties, Journal of Sedimentary Research, v. 81, n. 5, p. 339-347. DOI: 10.2110/jsr.2011.31.

Burton, D., & L.J. Wood, 2011, Quantitative shale characterization of the tidally influenced Sego Sandstone, AAPG bulletin, v. 95, n. 7, p. 1207-1226, DOI: 10.1306/12081010119.

Caers, J., & T. Zhang, 2004, Multiple-point Geostatistics: A Quantitative Vehicle for Integrating Geologic Analogs into Multiple Reservoir Models, in G.M. Grammer, Harris, P.M., Eberli, G.P., Integration of outcrop and modern analogs in reservoir modeling: AAPG Memoir 80, p. 383-394.

Campbell, C.V., 1976, Reservoir geometry of a fluvial sheet sandstone, AAPG Bulletin, v. 60, n. 7, p. 1009-1020.

Carle, S.F., E.M. Labolle, G.S. Weissmann, D. Van Brocklin, & G.E. Fogg, 1998, Conditional Simulation of Hydrofacies Architecture: a Transition Probability/Markov Approach, in Hydrogeologic Models of Sedimentary Aquifers, Concepts in Hydrogeology and Environmental Geology N. 1, SEPM Special Publication, ed. Fraser, G.S. and J.M. Davis, p. 147-170.

Chenoweth, W.L., 1998, Uranium Mining in the Morrison Formation, Modern Geology, v. 23, p. 427-439.

Chugunova, T. & L. Hu, 2008, Multiple-point statistical simulations constrained by continuous auxiliary data, Math Geosci, v. 40, n. 2, p. 133–146, DOI: 10.1007/s11004-007-9142-4.

Comunian, A., P. Renard, J. Straubhaar, & P. Bayer, 2011, Three-dimensional high resolution fluvio-glacial aquifer analog—Part 2: Geostatistical modeling, Journal of Hydrology, vol. 405, n. 1, p. 10-23, DOI: 10.1016/j.jhydrol.2011.03.037.

Comunian, A., P. Renard, & J. Straubhaar, 2012, 3D multiple-point statistics simulation using 2D training images, Computers & Geosciences, v. 40, p. 49-65, DOI: 10.1016/j.cageo.2011.07.009.

Comunian, A., S.K. Jha, B.M.S. Giambastiani, G. Mariethoz, & B.F.J. Kelly, 2014, Training Images from Process-Imitating Methods: An Application to the Lower Namoi Aquifer, Murray-Darling Basin, Australia, Math Geosci, v. 46, p. 241-260, DOI: 10.1007/s11004-013-9505-y.

Cowan, E.J., 1991, The Large-Scale Architecture of the fluvial Westwater Canyon Member, Morrison Formation (Upper Jurassic), San Juan Basin, New Mexico, in Miall, A.D., N. Tyler, The three-dimensional facies architecture of terrigenous clastic sediments, and its implications for hydrocarbon discovery and recovery, SEPM, Concepts in Sedimentology and Paleontology, v. 3, p. 80-93.

Dai, Z., R.W. Ritzi Jr., & D.F. Dominic, 2005, Improving permeability semivariograms with transition probability models of hierarchical sedimentary architecture derived from outcrop analog studies, Water Resources Research, v. 41, W07032, DOI: 10.1029/2004WR003515.

Davis, J. M., J. L. Wilson, F. M. Phillips, & M. B. Gotkowitz, 1997, Relationship between fluvial bounding surfaces and the permeability correlation structure, Water Resources Research, v. 33, n. 8, p. 1843–1854, DOI: 10.1029/97WR01003.

de Vries, L.M., J. Carrera, O. Falivene, O. Gratacos, & L.J. Slooten, 2009, Application of Multiple Point Geostatistics to Non-stationary Images, Mathematical Geosciences, v. 41, p. 29-42, DOI: 10.1007/s11004-008-9188-y.

Dickinson, W.R., & G.E. Gehrels, 2008, Sediment Delivery to the Cordilleran Foreland Basin: Insights from U-Pb Ages of Detrital Zircons in Upper Jurassic and Cretaceous Strata of the Colorado Plateau, American Journal of Science, v. 308, p. 1041-1082, DOI: 10.2475/10.2008.01.

Dimitrakopoulos, R., H. Mustapha, & E. Gloaguen, 2010, High-order statistics of spatial random fields: exploring spatial cumulants for modeling complex non-Gaussian and non-linear phenomena, Mathematical Geosciences, v. 42, n. 1, p. 65-99, DOI: 10.1007/s11004-009-9258-9.

Enge, H.D., S.J. Buckley, A. Rotevatn, & J.A. Howell, 2007, From outcrop to reservoir simulation model: Workflow and procedures, Geosphere, v. 3, n. 6, p. 469-490, DOI: 10.1130/GES00099.1.

ERDAS Imagine v. 11.0.1-.0.4, 2011.

Fabuel-Perez, I., D. Hodgetts, & J. Redfern, 2009, A new approach for outcrop characterization and geostatistical analysis of a low-sinuosity fluvial-dominated succession using digital outcrop models: Upper Triassic Oukaimeden Sandstone Formation, central High Atlas, Morocco, AAPG bulletin, v. 93, n. 6, p. 795-827, DOI: 10.1306/02230908102.

Falivene, O., P. Arbués, J. Howell, J. A. Muñoz, O. Fernández & M. Marzo, 2006, Hierarchical geocellular facies modelling of a turbidite reservoir analogue from the Eocene of the Ainsa Basin, NE Spain, Marine and Petroleum Geology, v. 23, n. 6, p. 679-701, DOI: 10.1016/j.marpetgeo.2006.05.004.

Feyen, L., & J. Caers, 2004, Multiple-point geostatistics: A powerful tool to improve groundwater flow and transport predictions in multi-modal formations, in P. Renard, H. Demougeot-Renard, and R. Froidevaux geoENV V: Geostatistics for Environmental Applications, p. 197–208, Springer Berlin Heidelberg, DOI: 10.1007/3-540-26535-X_17.

Fielding, C.R., J.P. Allen, J. Alexander, & M.R. Gibling, 2009, Facies model for fluvial systems in the seasonal tropics and subtropics, Geology, v. 37, p. 623-626, DOI: 10.1130/G25727A.1.

Fiocco, G. & L.D. Smullin, 1963, Detection of scattering layers in the upper atmosphere (60-140 km) by optical radar, Nature, v. 199, p. 1275-1276, DOI: 10.1038/1991275a0.

Fogg, G.E., 1986, Groundwater Flow and Sand Body Interconnectedness in a Thick, Multiple-Aquifer System, Water Resources Research, v. 22, n. 5, p. 679-694, DOI: 10.1029/WR022i005p00679.

García-Sellés, D., O. Falivene, P. Arbués, O. Gratacos, S. Tavani & J.A. Muñoz., 2011, Supervised identification and reconstruction of near-planar geological surfaces from terrestrial laser scanning, Computers & Geosciences, v. 37, n. 10, p. 1584-1594, DOI: 10.1016/j.cageo.2011.03.007.

Godin, P.D., 1991, Fining-upward cycles in the sandy braided-river deposits of the Westwater Canyon Member (Upper Jurassic), Morrison Formation, New Mexico, Sedimentary Geology, v. 70, n. 1, p. 61-82, DOI: 10.1016/0037-0738(91)90066-M.

Goovaerts, P., 1997, Geostatistics for Natural Resources Evaluation: Oxford, Oxford University Press, 483p.

GRASS Development Team, 2014, Geographic Resources Analysis Support System (GRASS) Software v. 6.4.4.: Open Source Geospatial Foundation Project, http: //grass.osgeo.org.

Guardiano, F.B., & M. Srivastava, 1993, Multivariate geostatistics: beyond bivariate moments, in Geostatistics Troia'92, Springer Netherlands, p. 133-144.

Hartzell, P., C. Glennie, K. Biber, & S. Khan, 2014, Application of multispectral LiDAR to automated virtual outcrop geology, ISPRS Journal of Photogrammetry and Remote Sensing, v. 88, p. 147-155.

Heinz, J., S. Kleineidam, G. Teutsch, & T. Aigner, 2003, Heterogeneity patterns of Quaternary glaciofluvial gravel bodies (SW-Germany): application to hydrogeology, Sedimentary Geology, v. 158, p. 1-23, DOI: 10.1016/S0037-0738(02)00239-7.

http://docs.opencv.org/modules/calib3d/doc/camera_calibration_and_3d_reconstruction.html.

http://wiki.blender.org/index.php/User:Shuvro/soc2011.

Hodgetts, D., 2013, Laser scanning and digital outcrop geology in the petroleum industry: a review, Marine and Petroleum Geology, v. 46, p. 335-354.

Hu, L. Y. & T. Chugunova, 2008, Multiple-point geostatistics for modeling subsurface heterogeneity: A comprehensive review, Water Resour. Res., v. 44, n. 11, DOI: 10.1029/2008WR006993.

Hu, R., R. Brauchler, M. Herold, P. Bayer, 2011, Hydraulic tomography analog outcrop study: Combining travel time and steady shape inversion, Journal of Hydrology, v. 409, p. 350-362, DOI: 10.1016/j.jhydrol.2011.08.031.

InnovMetric PolyWorks v. 11, 2011.

Jensen, J.R., 1996, Introductory Digital Image Processing: A Remote Sensing Perspective, 2nd ed., Prentice Hall, Upper Saddle River, NJ.

Johnson, N.M., & S.J. Dreiss, 1989, Hydrostratigraphic interpretation using indicator geostatistics: Water Resources Research, v. 25, p. 2501-2510, DOI: 10.1029/WR025i012p02501.

Kazhdan, M., & M. Bolitho, 2006, Screened Poisson Surface Reconstruction (Version 6.13): http://www.cs.jhu.edu/~misha/Code/PoissonRecon.

Kazhdan, M., M. Bolitho, & H. Hoppe, 2006, Poisson Surface Reconstruction, Proceedings of the fourth Eurographics symposium on Geometry processing, v. 7.

Kelly, T.E., 1977, Geohydrology of the Westwater Canyon member, Morrison Formation, of the southern San Juan Basin, New Mexico, in Guidebook to San Juan Basin III, New Mexico Geological Society, 28th Field Conference, p. 285-290.

Kernodle, J.M., 1996, Hydrogeology and steady-state simulation of ground-water flow in the San Juan Basin, New Mexico, Colorado, Arizona, and Utah, USGS Water-Resources Investigations Report 95-4187.

Klingbeil, R., S. Kleineidam, U. Asprion, T. Aigner, & G. Teutsch, 1999, Relating lithofacies to hydrofacies: outcrop-based hydrogeological characterization of Quaternary gravel deposits, Sedimentary Geology, v. 129, n. 3-4, p. 299-310, DOI: 10.1016/S0037-0738(99)00067-6.

Klise, K. A., G. S. Weissmann, S. A. McKenna, E. M. Nichols, J. D. Frechette, T. F. Wawrzyniec, & V. C. Tidwell, 2009, Exploring solute transport and streamline connectivity using lidar-based outcrop images and geostatistical representations of heterogeneity, Water Resources Research, v. 45, W05413, DOI: 10.1029/2008WR007500.

Knudby, C., & J. Carrera, 2005, On the relationship between indicators of geostatistical, flow and transport connectivity, Advances in Water Resources, v. 28, n. 4, p. 405-421, DOI: 10.1016/j.advwatres.2004.09.001.

Koltermann, C.E. & S.M. Gorelick, 1996, Heterogeneity in sedimentary deposits: A review of structure-imitating, process-imitating, and descriptive approaches, Water Resources Research, v. 32, n. 9, p. 2617-2658, DOI: 10.1029/96WR00025.

Kurz, T.H., S.J. Buckley, J.A. Howell, & S. Schneider, 2011, Integration of Panoramic Hyperspectral Imaging with Terrestrial Lidar Data, The Photogrammetric Record, v. 26, n. 134, p. 212-228, DOI: 10.1111/j.1477-9730.2011.00632.x.

Laskowski, A.K., P.G. DeCelles, & G.E. Gehrels, 2013, Detrital Zircon Geochronology of Cordilleran Retroarc Foreland Basin Strata, western North America, Tectonics, v. 32, p. 1027–1048, DOI: 10.1002/tect.20065

Lee, S., S.F. Carle, & G.E. Fogg, 2007, Geologic heterogeneity and a comparison of two geostatistical models: Sequential Gaussian and transition probability-based geostatistical simulation, Advances in Water Resources, v. 30, n. 9, p. 1914-1932, DOI: 10.1016/j.advwatres.2007.03.005.

Lopez S, A. Galli, & I. Cojan, 2001, Fluvial meandering channelized reservoirs: a stochastic and process based approach, In: IAMG annual meeting, Cancun, Mexico.

Maharaja, A., 2008, TiGenerator: Object-based training image generator, Computers & Geosciences, v. 34, p. 1753-1761, DOI: 10.1016/j.cageo.2007.08.012.8.

Martinsen, O.J., A.J. Pulham, P.D. Haughton, & M.D. Sullivan, 2011, Outcrops Revitalized: Tools, Techniques and Applications, and papers therein.

McLemore, V.T., & W.L. Chenoweth, 2003, Uranium Resources in the San Juan Basin, New Mexico, in Geology of the Zuni Plateau, New Mexico Geological Society, 54th Field Conference, p. 165-177.

Miall, A.D., 1985, Architectural-Element Analysis: A New Method of Facies Analysis applied to Fluvial Deposits, Earth-Science Reviews, v. 22, p. 261-308.

Miall, A. D., & C. E. Turner-Peterson, 1989, Variations in fluvial style in the Westwater Canyon Member, Morrison formation (Jurassic), San Juan basin, Colorado plateau, Sedimentary Geology, v. 63, p. 21-60, DOI: 10.1016/0037-0738(89)90070-5.

Miall, A.D., 1996, The Geology of Fluvial Deposits: Sedimentary Facies, Basin Analysis, and Petroleum Geology, Springer-Verlag Berlin Heidelberg New York, 582 p.

Nichols, E.M., G.S. Weissmann, T.F. Wawrzyniec, J.D. Frechette, & K.A. Klise, 2011, Processing of outcrop-based lidar imagery to characterize heterogeneity for groundwater models, SEPM concepts in sedimentology and paleontology, v. 10, p. 239-247.

OpenEXR, v. 2.0, 2013, www.openexr.com.

Phelps, G., & A. Boucher, 2009, Mapping Locally Complex Geologic Units in Three Dimensions: The Multi-Point Geostatistical Approach, Three-Dimensional Geological Mapping: p. 36-39.

Plink-Björklund, P., 2015, Morphodynamics of rivers strongly affected by monsoon precipitation: Review of depositional style and forcing factors, Sedimentary Geology, v. *323*, p. 110-147, DOI: 10.1016/j.sedgeo.2015.04.004.

Pringle, J.K., A.R. Westerman, J.D. Clark, N.J. Drinkwater, & A.R. Gardiner, 2004, 3D high-resolution digital models of outcrop analogue study sites to constrain reservoir model uncertainty: an example from Alport Castles, Derbyshire, UK, Petroleum Geoscience, v. 10, p. 343-352.

Pyles, D. R., D.C. Jennette, M. Tomasso, R.T. Beaubouef, & C. Rossen, 2010, Concepts learned from a 3D outcrop of a sinuous slope channel complex: Beacon Channel Complex, Brushy Canyon Formation, West Texas, USA, Journal of Sedimentary Research, v. 80, n. 1, p. 67-96, DOI: 10.2110/jsr.2010.009.

Pyrcz, M.J., J.B. Boisvert, & C.V. Deutsch, 2009, ALLUVSIM: A program for event-based stochastic modeling of fluvial depositional systems, Computers & Geosciences, v. 35, n. 8, p. 1671-185, DOI: 10.1016/j.cageo.2008.09.012.

Rarity, F., X.M.T. van Lanen, D. Hodgetts, R.L. Gawthorpe, P. Wilson, I. Fabuel-Perez, & J. Redfern, 2014, LiDAR-based digital outcrops for sedimentological analysis: workflows and techniques, Geological Society, London, Special Publications, v. 387, p. 153-183, DOI: 10.1144/SP387.5.

Renard, P., & D. Allard, 2013, Connectivity metrics for subsurface flow and transport, Advances in Water Resources, v. 51, p. 168-196, DOI: 10.1016/j.advwatres.2011.12.001.

Rittersbacher, A., J. A. Howell, & S.J. Buckley, 2014, Analysis of fluvial architecture in the Blackhawk Formation, Wasatch Plateau, Utah, U.S.A., using large 3D photorealistic Models, Journal of Sedimentary Research, v. 84, p. 72–87, DOI: 10.2110/jsr.2014.12.

Ritzi, R.W., Jr., 2000, Behavior of indicator variograms and transition probabilities in relation to the variance in lengths of hydrofacies, Water Resources Research, v. 36, p. 3375-3381, DOI: 10.1029/2000WR900139.

Rotevatn, A., S.J. Buckley, J.A. Howell, & H. Fossen, 2009, Overlapping faults and their effect on fluid flow in different reservoir types: A LiDAR-based outcrop modeling and flow simulation study: American Association of Petroleum Geologists Bulletin, v. 93, p. 407–721 427, DOI: 10.1306/09300807092.

Stone, W.J., 2003, Hydrostratigraphy, hydrodynamics, and hydrochemistry; geologic controls of ground-water phenomena in the San Juan Basin, in Geology of the Zuni Plateau, New Mexico Geological Society, 54th Field Conference, p. 191-195.

Strebelle, S., 2002, Conditional Simulation of Complex Geological Structures Using Multiple-Point Statistics, Mathematical Geology, v. 34, n. 1, p. 1-21.

Straubhaar, J., P. Renard, G. Mariethoz, R. Froidevaux, & O. Besson, 2011, An Improved Parallel Multiple-point Algorithm Using a List Approach, Math Geoscience, vol. 43, p. 305-328, DOI: 10.1007/s11004-011-9328-7.

Straubhaar, J., A. Walgenwitz & P. Renard, 2013, Parallel Multiple-Point Statistics Algorithm Based on List and Tree Structures, Mathematical Geosciences, v. 45, p. 131-147, DOI: 10.1007/s11004-012-9437-y.

Turner-Peterson, C.E., 1986, Fluvial sedimentology of a major uranium-bearing sandstone – a study of the Westwater Canyon Member of the Morrison Formation, San Juan Basin, New Mexico, in A Basin Analysis Case Study: Morrison Formation, Grants Uranium Region, New Mexico, AAPG Studies in Geology, v. 22, p. 47-75.

Turner-Peterson, C.E., & N.S. Fishman, 1986, Geologic Synthesis and Genetic Models for Uranium Mineralization in the Morrison Formation, Grants Uranium Region, New Mexico, in A Basin Analysis Case Study: Morrison Formation, Grants Uranium Region, New Mexico, AAPG Studies in Geology, v. 22, p. 357-388 .

Turner, C.E., & F. Peterson, 2004, Reconstruction of the Upper Jurassic Morrison Formation extinct ecosystem – a synthesis, Sedimentary Geology, v. 167, n. 3, p. 309-355, DOI: 10.1016/j.sedgeo.2004.01.009.

Vassena, C., L. Cattaneo, & M. Giudici, 2010, Assessment of the role of facies heterogeneity at the fine scale by numerical transport experiments and connectivity indicators, Hydrogeology journal, v. 18, n. 3, p. 651-668, DOI: 10.1007/s10040-009-0523-2.

Viseur, S., R. Richet, & J. Borgomano, 2007, Semi-automated detections of geological features from DOM – The Gresse-en-Vercors Cliff, 69th EAGE Conference and Exhibition.

Weissmann, G.S., & G.E. Fogg, 1999, Multi-scale alluvial fan heterogeneity modeled with transition probability geostatistics in a sequence stratigraphic framework, Journal of Hydrology, v. 226, n. 1-2, p. 48-65, DOI: 10.1016/S0022-1694(99)00160-2.

Weissmann, G.S., S.F. Carle, & G.E. Fogg, 1999, Three-dimensional hydrofacies modeling based on soil surveys and transition probability geostatistics, Water Resources Research, v. 35, n. 6, p. 1761-1770, DOI: 10.1029/1999WR900048.

Weissmann, G.S., Y. Zhang, G.E. Fogg, & J.F. Mount, 2004, Influence of incised valley fill deposits on hydrogeology of a glacially-influenced, stream-dominated alluvial fan, in Bridge, J., and Hyndman, D.W., Aquifer Characterization, SEPM Special Publication 80, p. 15-28.

Weissmann, G.S., A. Pickel, K.C. McNamara, J.D. Frechette, I. Kalinovich, R. M. Allen-King, & I. Jankovic, in press, Characterization and quantification of aquifer heterogeneity using outcrop analogs, GSA Bulletin, DOI: 10.1130/B31193.1.

Whittaker, J., & G.Teutsch, 1999, Numerical simulation of subsurface characterization methods: application to a natural aquifer analogue, Advances in Water Resources, v. 22, n. 8, p. 819-829, DOI: 10.1016/S0309-1708(98)00056-6.

Xu, X., C.L. Aiken, J.P. Bhattacharya, R.M. Corbeanu, K.C, Nielsen, G.A. McMechan & M.G. Abdelsalam, M. G., 2000, Creating virtual 3-D outcrop, The Leading Edge, v. 19, n. 2, p. 197-202, DOI: 10.1190/1.1438576.

Zappa, G., R. Bersezio, F. Felletti, & M. Giudici, 2006, Modeling heterogeneity of gravel-sand, braided stream, alluvial aquifers at the facies scale, Journal of Hydrology, v. 325, p. 134-153, DOI: 10.1016/j.jhydrol.2005.10.016.